(1)

Quarterly Progress Report #3
4/01/92 - 6/30/92

Field Emitter Array RF Amplifier Development Project
Phase One, Cathode Technology Development
DARPA Contract #MDA 972-91-C-0028

Sponsored by:
Dr. Bertram Hui
DARPA/DSO

MCNC, Center for Microelectronics
Post Office Box 12889
Research Triangle Park, NC 27709-2889

Gary Jones, Principal Investigator

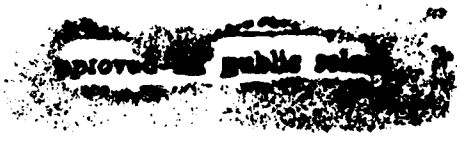

REPORT DOCUMENTATION PAGE

Form Approved
OMB No. 0704-0188

1. AGENCY USE ONLY (*Leave blank*)	2. REPORT DATE	3. REPORT TYPE AND DATES COVERED
	APR 92	QUARTERLY, 4/01/92 – 6/30/92

4. TITLE AND SUBTITLE
Quarterly Progress Report #3: 4/01/92 – 6/30/92

5. FUNDING NUMBERS
C
MDA972-91-C-0028

6. AUTHOR(S)
Dr. Ching-Tzong Sune
Gary W. Jones, Principal Investigator

7. PERFORMING ORGANIZATION NAME(S) AND ADDRESS(ES)
MCNC Electronic Technologies Division
Post Office Box 12889
3021 Cornwallis Road
Research Triangle Park, North Carolina 27709-2889

8. PERFORMING ORGANIZATION REPORT NUMBER
P9250004-Q3

9. SPONSORING ORGANIZATION NAME(S) AND ADDRESS(ES)
ARPA/DSO
3701 North Fairfax Drive
Arlington, Virginia 22203-1714

10 SPONSORING/MONITORING AGENCY REPORT NUMBER

11. SUPPLEMENTARY NOTES
Dr. Sune (919) 248-1975, (919) 248-1455 FAX
COTR: Dr. Bertram Hui (703) 696-2239, (703) 696-2201 FAX

12a. DISTRIBUTION/AVAILABILITY STATEMENT
Approved for public release; distribution is unlimited.
Defense Technical Information Center
Building 5 / Cameron Station
Arlington, Virginia 22214

12b. DISTRIBUTION CODE

13. ABSTRACT (*Maximum 200 words*)

Third Quarterly R&D Status / Technical report for the Field Emitter Array RF Amplifier Development Project - Phase I, Cathode Technology Development.

14. SUBJECT TERMS
Field emission, cold cathode, RF amplifier

15. NUMBER OF PAGES
43

16. PRICE CODE

17. SECURITY CLASSIFICATION OF REPORT	17. SECURITY CLASSIFICATION OF THIS PAGE	17. SECURITY CLASSIFICATION OF ABSTRACT	20.LIMITATION OFABSTRACT
UNCLASSIFIED	UNCLASSIFIED	UNCLASSIFIED	

Quarterly Progress Report #3
(4/01/92 - 6/30/92)

Sponsored by: Dr. Bertram Hui
DARPA/DSO
3701 N. Fairfax Drive
Arlington, VA 22203
(703) 696-2239

Contractor: MCNC, Center For Microelectronics
Post Office Box 12889
3021 Cornwallis Road
Research Triangle Park, North Carolina, 27709-2889

Effective Date of Contract: 9/09/91

Contract Expiration Date: 3/09/93

Contract Amount: Basic $1,178,466.00

Principal Investigator: Gary Jones
919-248-1922, FAX: 919-248-1455

Title of Work: Field Emitter Array RF Amplifier Development Project
Phase One, Cathode Technology Development
DARPA Contract #MDA 972-91-C-0028

MCNC Field Emitter Array RF Amplifier Development Program

Phase One, Cathode Technology Development - DARPA Contract MDA 972-91-C-0028

Third Quarter - July 1992

Key Ideas

Develop microstructural field emission diodes with a cutoff frequency above 1 GHz, 5A/cm^2 at <200V G-E bias, and >100hr lifetime.

Reduce capacitance and increase transconductance of FEA devices to improve frequency response. Primarily use tall emitter columns surrounded by SiO_2 to reduce capacitance. Evaluate low work function emitter surfaces, small gate dimensions, and improved tip radius control to improve transconductance.

Evaluate various anode configurations including vacuum microencapsulation to permit testing of larger numbers of sample FEA devices.

Model and characterize our versions of the FEA device toward implementation in an RF amplifier.

Major Accomplishments:

Several gated field emitter-on-a-column structures with low capacitance and improved gate-emitter isolation have been successfully fabricated. Testing has indicated additional effort is required to improve transconductance.

Variations of the above columns with sharper points are in process.

Samples of our column emitters, standard emitters, and flat gated cathodes have been sent to several vendors for diamond and diamond-like depositions.

New vacuum test systems for field emitters have just been constructed at NCSU and UNC-Charlotte.

Field-ion micrographs and electron emission patterns have been studied for our emitters under a variety of conditions.

Amplifier modules containing our gated emitters have been constructed at Litton LSSD and testing methods for the modules are

MCNC Silicon Field Emitter with Column

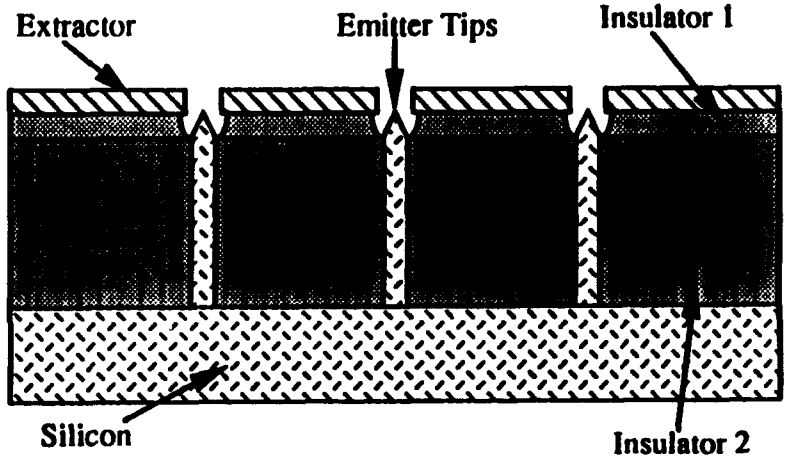

Major Milestones - This quarter and upcoming quarter

Construction of low capacitance gated FEA structure with 1.2-1.4 micron gates with modified gate-emitter isolation structure and initial testing is complete. Followup testing of modified structures planned for next quarter.

Obtain g_m/C suitable for 1 GHz (targeted 9/92)

Insertion of FEAs in macroscale tubes (planned 3/92 - now planned for 8/92) - Task expanded to both triodes and microstrip cavities. Large tube insertions planned for 9/91

Delivery of vacuum microencapsulation system (planned 4/92 - delayed until 8/92), Complete setup of vacuum microencapsulation system (planned 9/92 - delayed 1 month)

Field Emitter Array RF Amplifier Development Project
Phase 1, Cathode Technology Development

I. Executive Summary

All parallel R&D activities are now producing results. Fabrication of our low capacitance column emitter array structure is complete and in the process is being refined to improve transconductance. Our primary test apparatus are qualified and on line. Modeling efforts are showing results and being evaluated.

- Gated field emitter-on-a-column structures with low cell capacitance have been successfully fabricated with a modified gate-emitter isolation structure aimed at minimizing Frankle-Pool leakage and improving device stability. Columns of 6 microns final height were built based on data indicating the taller columns were of marginal added benefit. Testing of these devices yielded lower emission current than anticipated, based on micrographs and prior work with similar emitters. Tip sharpness may have been exaggerated by the SEM. Variations on this structure with cone angle modifications and secondary oxidation sharpening tests are in process which should provide sharper points and improved emission. Samples have also been sent out for low work function coatings, including diamond coating.

- A microstrip packaging methodology has been successfully designed to null capacitance in FEAs for narrow band, high frequency applications. The first pass mathematical model for this approach using field emitters was completed in May and the results are included. Efforts were shifted to solely field emitter array based broadband amplifier modeling. A report on the initial results of this effort is also attached.

- The UNC Charlotte vacuum testing system is complete. This system will be used for experimental noise studies of field emitter arrays as related to background gases and temperature. Additional development of an understanding of theoretical noise and emission stability mechanisms are also continuing.

- Trajectory analysis of our gated and ungated field emitters has been performed with clean and contaminated tips. Anode hysteresis effects previously observed by SRI and the NRL on oxidized anodes have now been observed on the NCSU test system with stainless steel anodes. Parallel experiments are planned to better understand and control this effect.

- Field ion imaging and electron imaging of our emitters has been performed. The initial results of this work are enclosed. This test method provides a more in depth experimentally based understanding of emission from these devices. The second test system at NCSU has just been completed. This system will provide us with improved emitter imaging capability.

- Hybrid modules for performing RF testing of our devices have just been completed at Litton by the solid state division. Our FEAs have been inserted in these modules. Testing methodologies for these modules in a vacuum are being developed at the Litton electron devices division.

II. Milestone Status:

Task	Completion Date	
	Original	Complete Expected
Complete first diodes of each of the three device types: Horizontal, vertical, and trench. Deliver samples to NRL, NCSU, and Litton. (MCNC)	11/91	11/91
Prepare first pass device models and potential circuit models based on initial device IV data. (Duke, MCNC, and UNC-CH)	3/92	11/92
Down select RF FEA designs based on device performance predictions	3/92	12/91
Complete first generation of field emission IV curves for each of the device types fabricated along with initial electron trajectory data and electron time of flight data. (NCSU and MCNC)	3/92	3/92 & Continuing
Design and order vacuum sealing and test system (MCNC)	11/92	12/91
Modify Litton trajectory modeling programs for field emission. Initial macroscale high vacuum tube encapsulation of field emission cathodes. (Litton)	3/92	11/91
Complete second set of field emission diode device runs with column FEAs (MCNC)	3/92	3/92
Complete third series of gated column emitters with modifications for very low electric fields over gate emitter isolations to reduce gate leakage	-	5/92
Complete new mask set for half micron field emission devices. (MCNC)	5/92	3/92
Install vacuum sealing and test system (MCNC) MCNC set-up a temporary vacuum test system in a SEM (3/92)	3/92	8/92 *
Complete initial electron trajectory modeling and initial testing of macroscale tubes containing microstructural gated FEC diodes. (Litton)	7/92	8/92
Complete fabrication of first microencapsulated FEC transistors. (MCNC)	9/92	11/92*
Generate first pass transistor data from microencapsulated FE transistors. (MCNC, Duke, and Litton)	9/92	12/92*
Demonstrate microstructural FEA diode/open triode devices meeting device IV and g_m/C program requirements.	9/92	9/92
Determine priorities of future device development. Determine the primary amplifier design methodology from the three amplifier design approaches. (MCNC)	9/92	9/92
Complete design for first integrated FEC based RF amplifier and FEC tube RF amplifier based on device characterizations. (MCNC, Duke, and Litton)	3/93	3/93
Complete second level models for FEC emission from surfaces treated in various manners. (UNC-CH)	3/93	3/93
Complete testing of FEC electron trajectories, electron trajectory model verification. (NCSU, Litton)	3/93	3/93
Determine packaging and cooling requirements for the prototype RF amplifier. (MCNC and Litton)	3/93	3/93

* Delivery of vacuum sealing system delayed by manufacturer

III. Technical Progress:

1.0 Theoretical FEA device developments

1.1 UNC Noise Modeling It is known experimentally from the work of Gomer et al, of Swanson et al, and of Gray et al, that electron field emission is effected in amplitude and angle by the presence and surface migration of adatoms on the emitting areas. Greene et al then proposed that noise measurements could help distinguish between mechanisms on silicon field emitters: specifically whether emission was from isolated atoms or large numbers of atoms, or somewhere in between.

The work carried out in the past quarter has resulted in a simple theoretical method which allows a calculation of the excess noise produced by individual adatoms on an emitter crystal surface, both for metal emitters and for silicon emitters. The purpose of the work was not to attempt a highly quantitative numerical analysis and simulation: the present state of the theory does not permit this. Instead, the purpose was to produce a method which would indicate the role of various important emission effects to be compared with later experimental emission and noise measurements, and to do so with both simplicity and high level of confidence. This work is not yet complete, but the outline and the direction of future work will be given below.

The original theory of Fowler and Nordheim and their many followers has been to use WKB methods to analyze the transmission of electrons through one dimensional barriers or through barriers of curvature much larger than atomic size. These methods are not quantitative for several reasons: (a) they do not use the actual Bloch wave structure of the electrons in the emitter interior or of surface states or surface resonances; (b) they do not properly account for the effects of exchange at the barrier "potential;" (c) they do not account for surface defects, adatoms, etc. Also one does not see in these theories the effect of the work function differences between different crystal faces. These are all effects which are known to workers in such fields as field-ion-microscopy and dynamic low energy electron diffraction (LEED I-V).

We now describe our initial theoretical method, which is treat the problem from the scattering viewpoint, in which the unperturbed wave functions are those describing field emission from a crystal plane, i.e., with incident and reflected waves within the crystal and a small transmitted wave tunneling into the high electric field outside. The scattering perturbation is the potential representing the adatom, and first order perturbation theory is used.

It is well-known that adatoms are strongly polarized on crystal surfaces by the 2-5 eV work function step which occurs over a distance of only a few Å: this is equivalent to a polarizing field of about 10^8 V/cm. This means that adatoms must be strongly polarized dipoles, and that the scattering of the Fowler-Nordheim wave function is not spherically symmetric, there is a strong local dipole scattering effect.

It should also be noted that the (+) side of the dipole is outward-facing, so that the barrier is lowered near the adatom. Furthermore, when it is realized that for an ideal crystal surface only the normal momentum is effective in tunneling, it can be seen that the relaxation of the transverse momentum conservation selection rule by the adatom potential increases the number of filled Bloch states near the Fermi level which can be emitted, by scattering grazing electrons into near-normal directions. These two effects will both increase the tunneling transmission rates and also increase the angular spread of emitted electrons. [The latter effect may have an adverse effect on beam quality.] Therefore any reasonable theory, or simulation of physically valid model, will show a current increase step at the moment of adatom adsorption, and a corresponding drop at the desorption step. This has to be the strongest mechanism of telegraph noise, calling for improvements in residual gas control, or by some other means of damping emission fluctuations. The latter possibility will be discussed in a subsequent report.

In the following sketch we indicate these factors

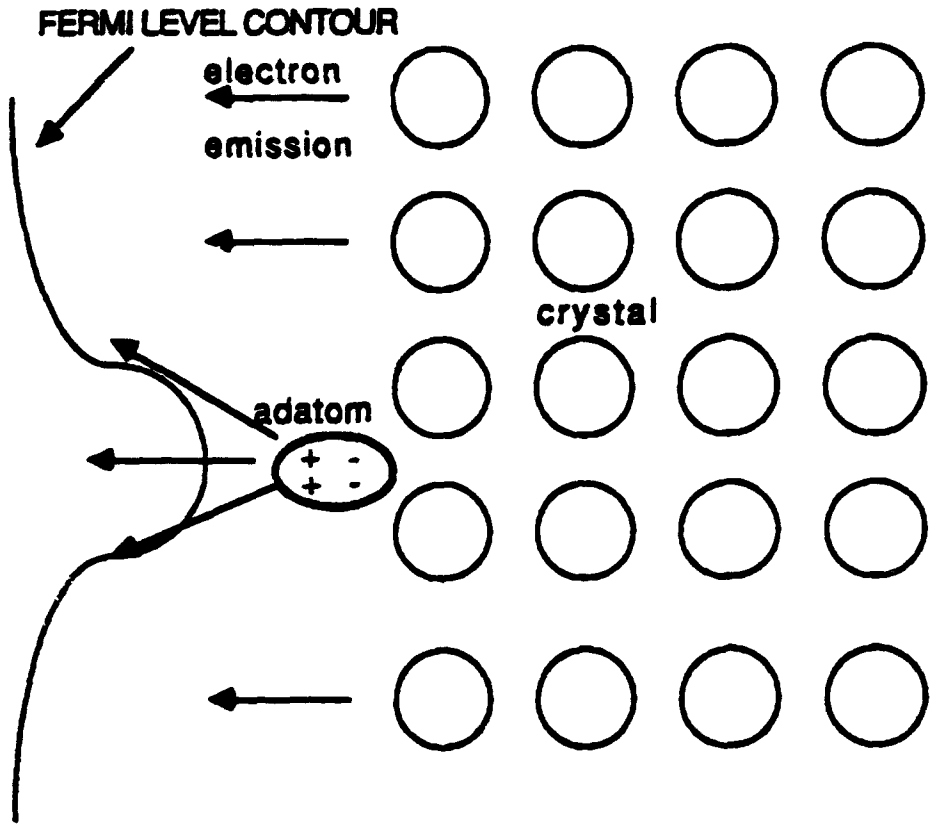

The calculation of these effects is being prepared for publication, including numerical evaluation of the results, and the completed paper will be included in the next quarterly report.

It appears that the model is strong enough to correlate the residual gas pressure with the noise, and thus to provide a fairly direct measure of emitting area, resolving a question that has remained a matter of dispute for many years.

1.2 An analysis of amplifier design parameters using field emitters is provided in Attachment A from Duke University.

1.3 Trajectory Computer Simulation of Field Emission, Litton EDD

The computer simulation code DEMEOS has been further modified by Dr. Richard True to include very special effects, observed and measured not to be smooth (or of smooth curvature variation) but to possess and display tiny microcrystals which protrude from the otherwise smooth tips of the field emitter. These recently observed and clarified microcrystal effects have been incorporated into the code DEMEOS. Computational data related to SRI and MCNC vacuum field emitter arrays have been generated and a report and paper is in preparation. An abstract, copy appended to this quarterly report, has been submitted to the International Electron Devices Meeting to be held in San Francisco, California in December 1993 . Work in this area continues. A copy of a abstract proposed for the 1993 IEDM by Richard True (Litton EDD) is attached as Attachment B.

2.0 Field Emitter Development

2.1 Fabrication of columnar gated emitters

Gated columnar emitters have been fabricated which are imbedded in a silicon dioxide matrix. These devices have 6 micron high columns which were previously modeled to be within 20-30% of the theoretical minimum-per-cell capacitance for a given gate-to-emitter spacing. These devices have gate openings of ~1.4 micron and were expected to turn on in the 50V-60V range based on

other small gated devices previously fabricated. SEMs of this final structure are shown in Figure 1. Early testing of these gated column emitters provided under 0.1 microamp per emitter at 300V gate to emitter. We anticipate these tips may be less sharp than indicated from the SEMs. We are in the process of testing added sharpening of these emitters and coating the samples with low work function coatings. These tests are still in process, as is a followup run with taller and sharper cones on the columns.

2.2 I-V characterizations of Si emitters

Field emission currents and images have been obtained from single gated emitters and from small arrays. For the purpose of relating the study of electron trajectories to emission current, we have concentrated on single emitters. Each silicon emitter has a typical radius of curvature estimated at less than 30 nm and a 2μm-diameter opening metal extraction gate, as shown by SEM investigation (Figure 2). Total emission currents of 1 to 2 microamps per emitter have been collected in the Faraday cup (anode) at extraction voltages of about 150 volts. A part of the experimental setup in our FIM system is shown in Figure 3. The emitter is pointed to the positively biased Faraday cup during the I-V measurement. The distance between the emitter and the anode is about 6 mm. Figures 4 and 5 show I-V curves and the corresponding Fowler-Nordheim plots for two individual emitters. Long term emission from those emitters has also been observed at modest vacuums. Parallel emitter testing is underway at NCSU, the NRL, and MCNC.

2.3 Emission test for the triode performance at NCSU

Under stable operating conditions, the emission current collected at the anode changes dramatically with anode bias. As Figure 6 shows, very little can be detected at the zero-biased anode. All the emitted current is drained through the gate. As the anode bias increases, the anode current approaches the full base current very quickly. This triode like property is expected to be more significant if we can shorten the distance between gate and anode. Another interesting feature found in this study is the hysteretic behavior of the anode current. The current ratios of the gate and the anode are also hysteretic when the anode voltage was raised up and decreased back, as shown in Figure 7. We consider this a complex effect involving the electric field and charge transfer between the gate and the anode, possibly involving a surface oxide on the anode.

2.4 Field emission imaging for the electron trajectories at NCSU

By pointing the emitter to the Chevron microchannel plates (MCP) fiberoptic imaging assembly, which in Figure 2, field emission images are obtained continuously as the emission current changes. Imaging distances, of 20 to 50 mm between the emitter and imaging assembly, have been used to study the emission patterns. Figure 8 shows emission images under three different extraction voltages. The size and the intensity of the image were found to change significantly with the gate voltage. In addition, the non-uniform electric field between the gate and the imaging assembly is responsible for further spreading of the electron beam (Figure 9). The emitting half angle from this pyramidal Si field emitter, shown by our preliminary investigations, is below 12° under moderate operating condition.

2.5 Emission from the silicon tip at NCSU

In order to understand the emission pattern of the Si emitter, field emission from a cleaned Si tip surface has been studied. Figure 10 shows a field emission image of a <111> oriented Si tip in the UHV background. By comparing with emission images of the Si emitter, it can be seen that the uniform emission patterns of the silicon emitter are the result of contamination and the native oxide layer on the emitter surface.

3.0 Vacuum Sealing/Testing System Design

3.1 Work on this program has been delayed due to a delay in the delivery of the vacuum sealing tool. This tool is now scheduled to arrive in August.

4.0 Other Developments

4.1 The development on the new test system at NCSU

The new multi-purpose field emission analytical vacuum system has been completely constructed and is being tested. Its vacuum is controlled by a 240 l/s Balzers turbomolecular pump and another Varian StarCell ion pump. Manual and electropneumatic gate valves have been used between the vacuum chambers and the pumps. Figure 11 shows a photograph of the whole system. A 10^{-7} torr range vacuum has been achieved in this new system without extensive bakeout. Further testing and improvements in the vacuum are expected shortly. The imaging device and other electronic parts are also being installed into the chamber. Elaborate designs and fabrication of the sample loading and supporting are further needed by considering the thermal conduction and high voltage isolations.

4.2 Using funds provided by the College of Engineering, an ultrahigh vacuum system has been designed and built under the direction of Professor Daneshvar, assisted by UNCC graduate student Mayya Deepak, who is supported under this program. The system is an all stainless steel conflat flange system, based on a 6-way cross, and pumped by two Varian turbomolecular pumps in series, backed by a Welsh-type vane pump. The system also has a load lock and transfer-rod arrangement. Samples can be rapidly introduced into the load-lock where they can undergo preliminary processing, then admitted to the ultrahigh vacuum chamber where emission measurements can be carried out. It is planned to provide calibrated gas exposure facilities so that ambient effects can be studied, as well as surface treatments of the emitter tips, which are being fabricated at MCNC under this contract.

The graduate student, Mr. Deepak will be compiling a listing and analysis of the relevant literature in this field, as part of the project.

4.3 Chip Preparation, Mounting and Vacuum Test Station, Litton EDD

The design of a base to place and hold in the vacuum chambers the mount ships produced by LSSD is nearly complete. The vacuum chamber has been operated and leaks in the rough-pump station are being fixed. DC data is expected by the middle of August.

Concurrently, Litton has carried out a design for a base to place and hold the mounted chips for the RF test using the features present on the old batch of mounted chips. This design activity has indicated solutions to issues anticipated in the RF tests. Litton LDD has interacted with Litton LSSD to jointly address and solve the RF mounting and test problems. Litton is looking at the total RF problem of the external circuit plus the mounted chip circuit as a single RF entity for the purpose of the planned RF measurements.

IV. Fiscal Status

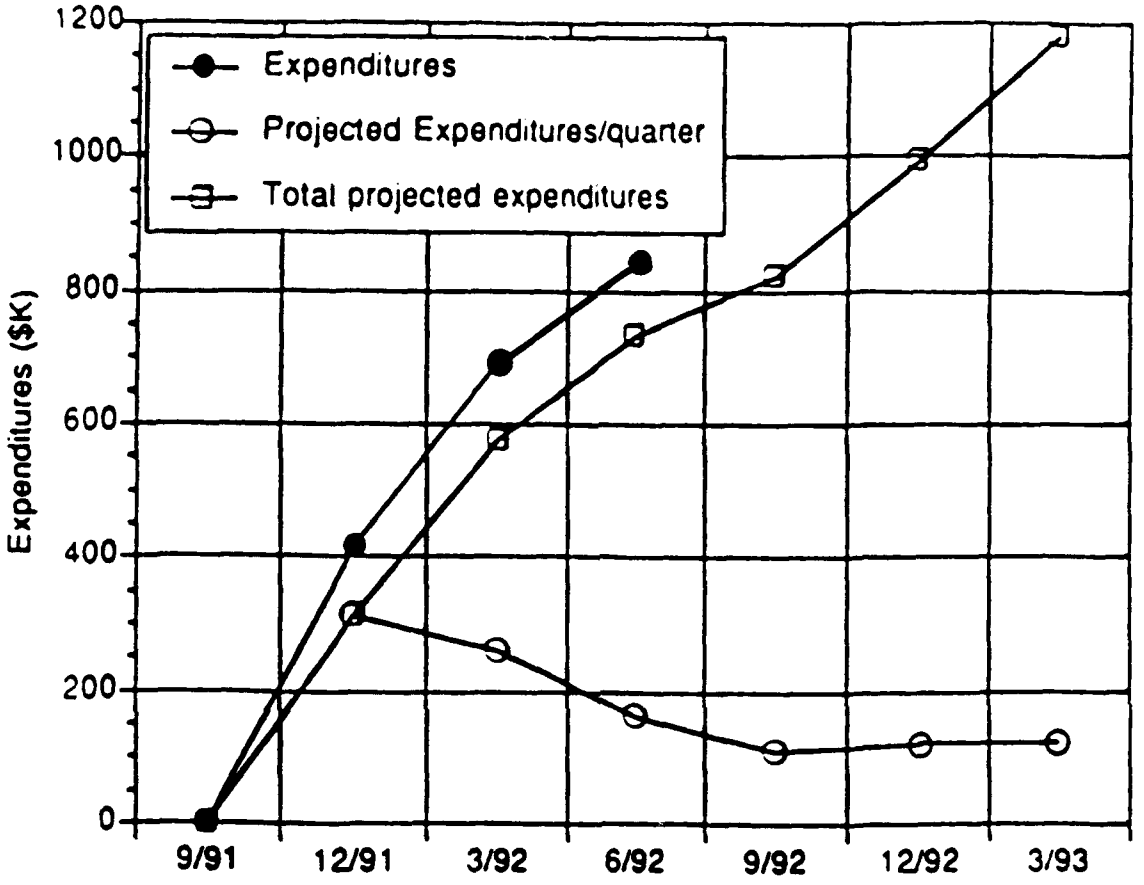

Expenditures this quarter (4/01/92 - 6/30/92)	$142,133.34
Total expenditures to date (9/09/91 - 6/30/92)	835,985.37
Projected expenditures:	
7/92 - 9/92	107,012.63
10/92 - 12/92	117,734.00
1/93 - 3/93	117,734.00
Contract Amount (Basic)	$1,178,466.00*

[*of this amount, funding of $1,072,000 has been authorized through February 15, 1993]

V. Problem Areas

The initial 1 GHz objective still appears achievable with our current device design and emitter material selection, although we must increase the performance of our gated column emitters to that of our small gated emitters based in ≤0.6 micron lithography. Lower work function coatings are needed to provide a margin for error in increasing transconductance. This work is progressing rapidly. With our various test vehicles now in place, we are nearing achieving this goal, but we still must correct for the degraded electron emission observed on our first gated column emitters.

VI. Visits and Technical Presentations

Presentations were made on our previously fabricated Thin Film Encapsulated Micro-Triodes, and our to the Electronics Components and Technology Conference (ECTC) in San Diego as well as to the International Vacuum Microelectronics Conference (IVMC) in Vienna Austria. A poster presentation was made at the IVMC for NCSU with related work on 'An Imaging Study of Electron Trajectories of Silicon Field Emitters'. All presentations related to DARPA sponsored activities referenced DARPA's support. No visits to the program occurred.

THIS
PAGE
IS
MISSING
IN
ORIGINAL
DOCUMENT

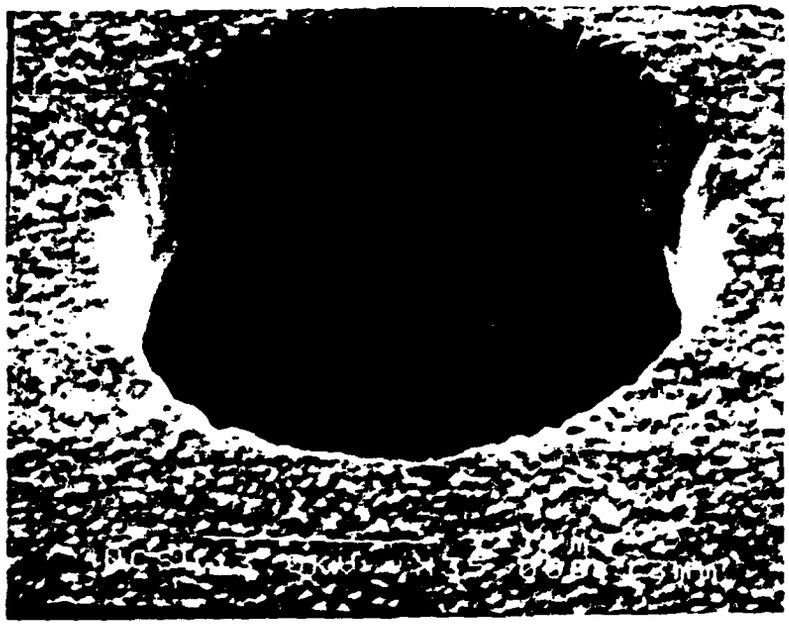

Figure 2: SEM Micrograph of a single Si field emitter

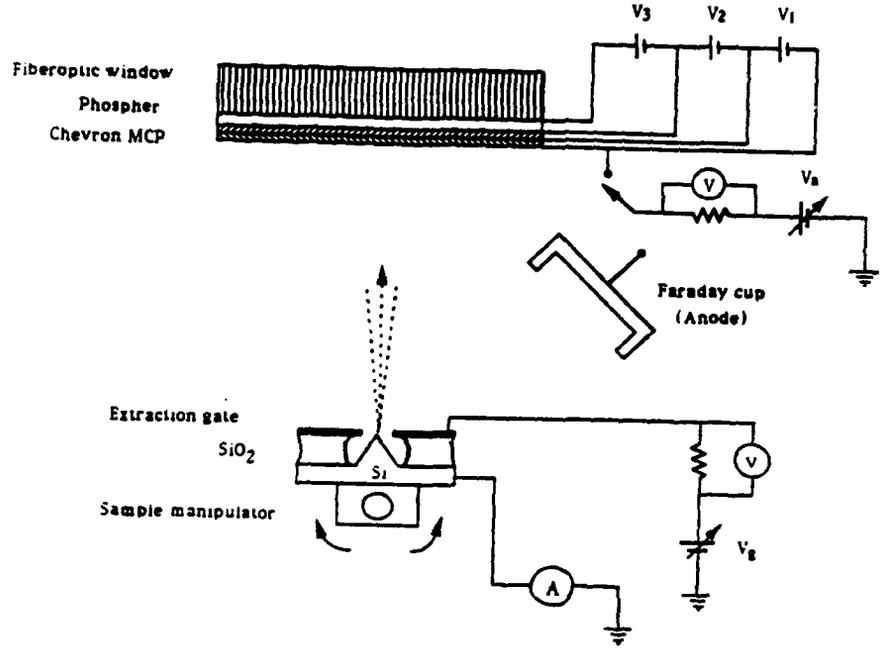

Figure 3: Schematic of the setup used in Si field emitter study

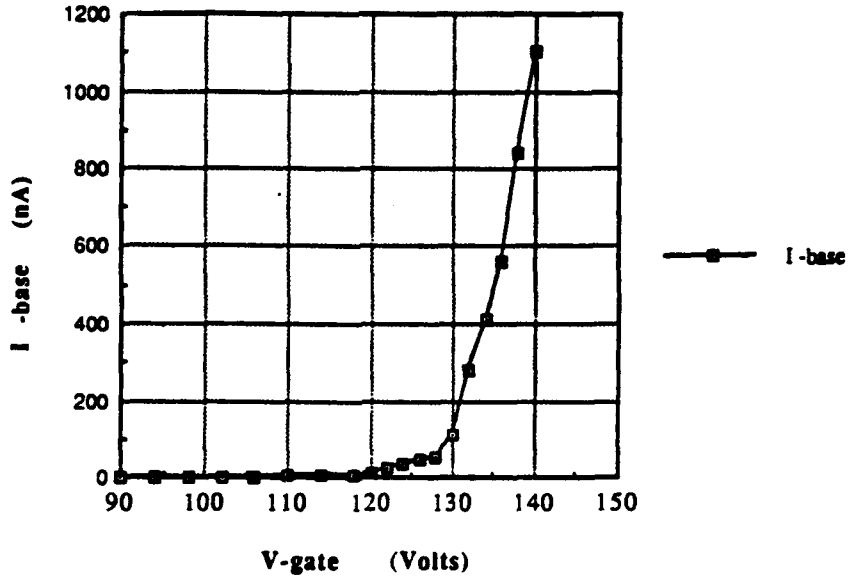

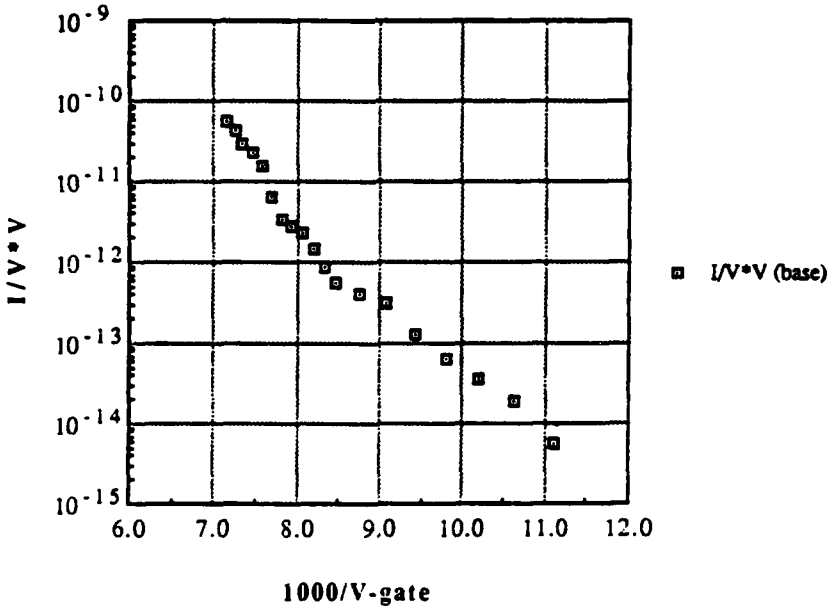

Figure 4: I-V characteristics and F-N plot of single Si field emitter No. 1.

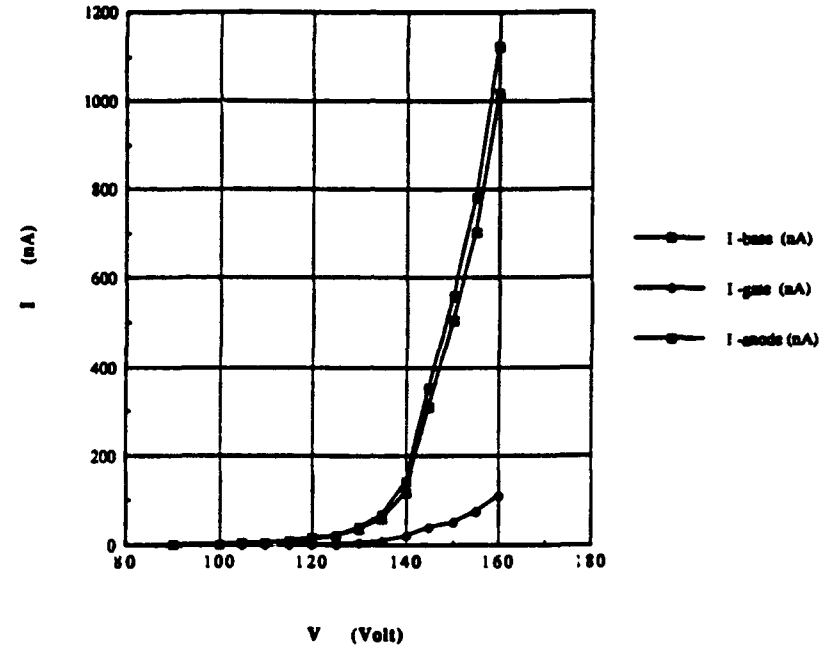

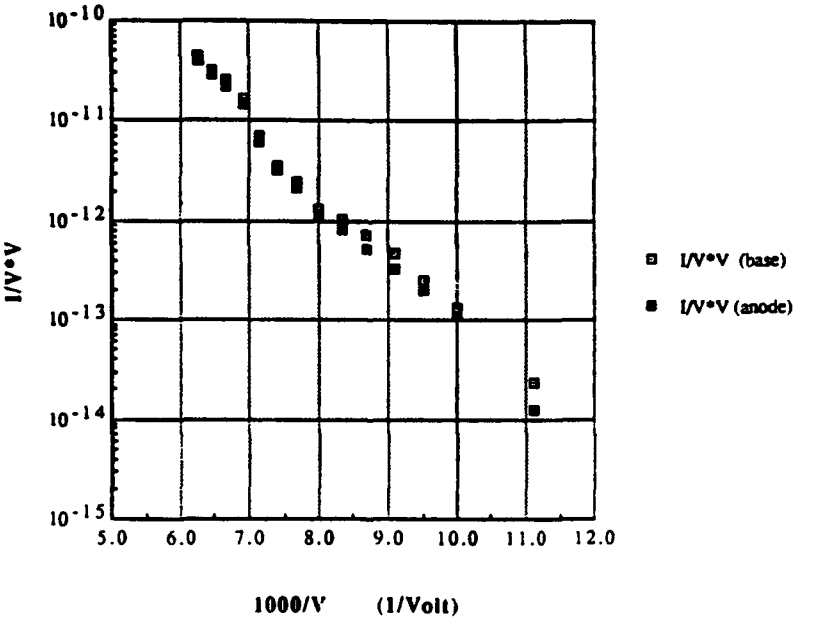

Figure 5: I-V characteristics and F-N plot of single Si field emitter No. 2.

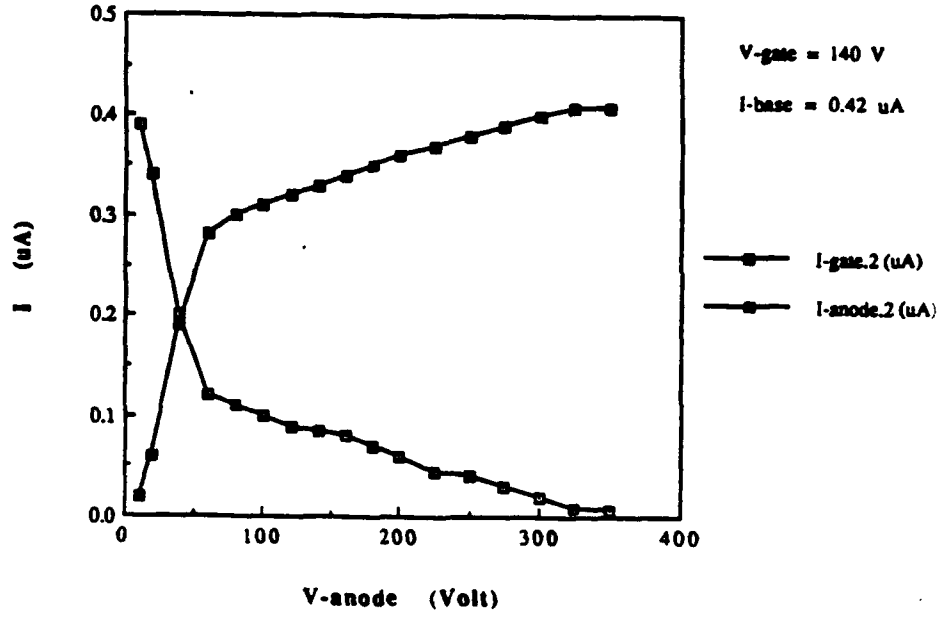

Figure 6: The anode current-voltage characteristics of the emitter No. 2.

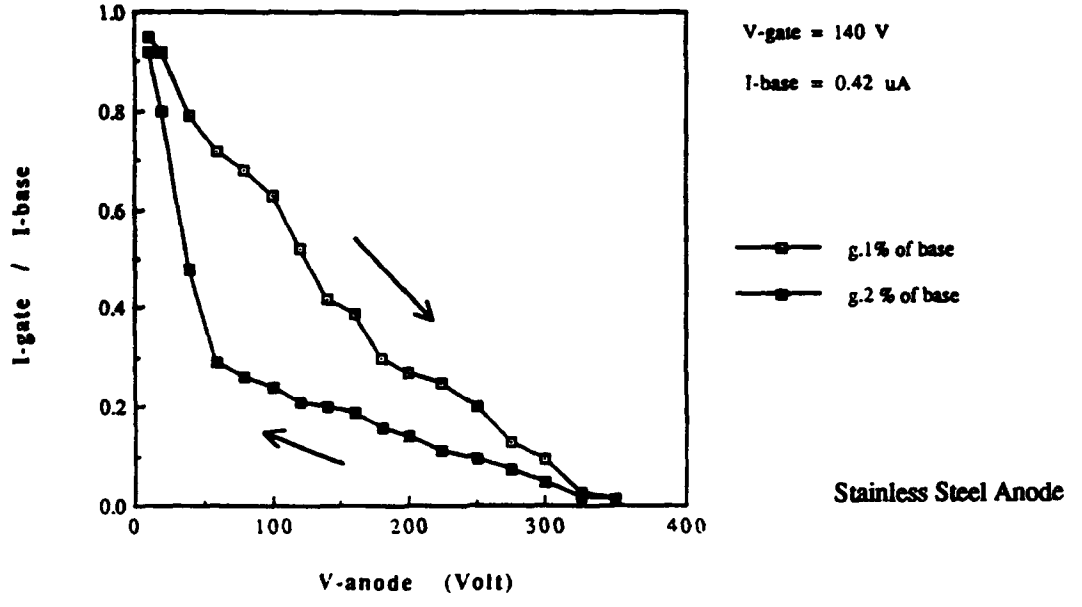

Figure 7:
The gate-base current ratio shows a hysteresis with the anode voltage

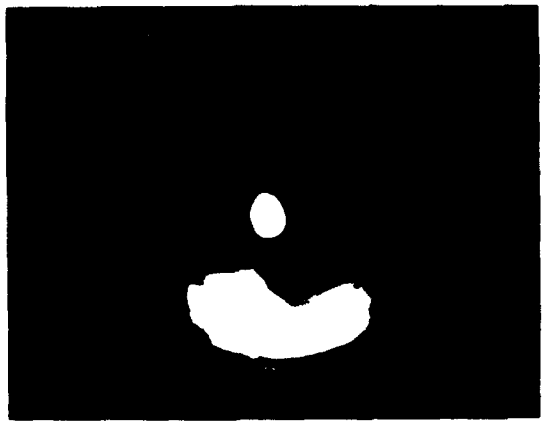

(a) V_{gate} = 90 V
$I_{emission}$ = 80 pA

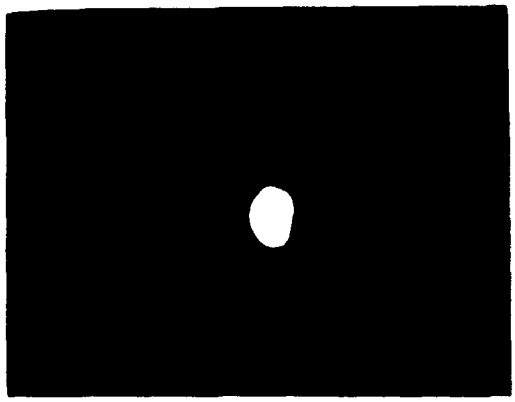

(b) V_{gate} = 100 V
$I_{emission}$ = 1.0 nA

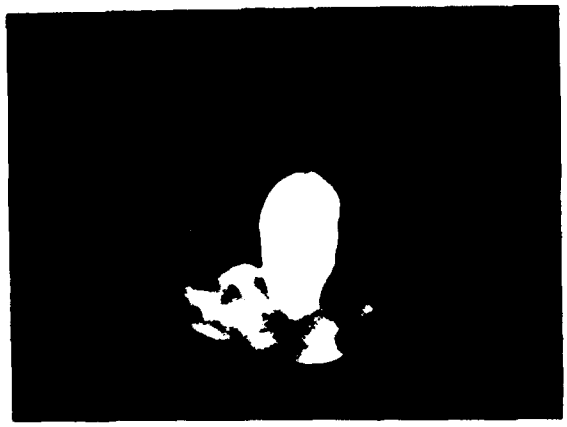

(c) V_{gate} = 120 V
$I_{emission}$ = 20 nA

Figure 8
Field emission images of the single Si emitter at the anode voltage of 400 volts and imaging distance of 40 mm.

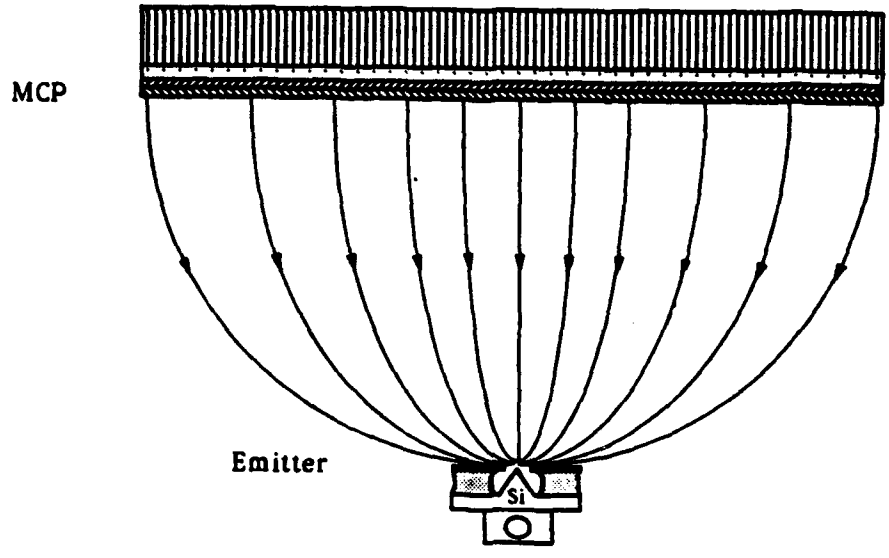

Figure 9: The electric field distribution between the gate and the anode.

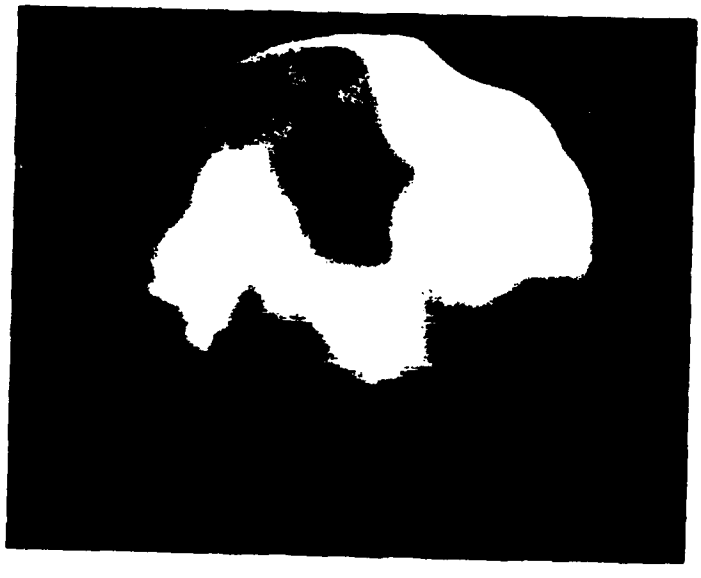

Figure 10: A field emission pattern from a <111> Si tip.

ATTACHMENT A

QUARTERLY REPORT ON FIELD-EMITTER AMPLIFIER RESEARCH

Joseph E. Mancusi, M.S. and William T. Joines, Ph.D.

Department of Electrical Engineering
Duke University
Durham, NC 27706

Project Period: April 1, 1992 - June 30, 1992

Chapter 1

Introduction

Our current progress on four separate tasks is discussed in Chapters 2, 3, 4, and 5. Chapter 2 discusses a finite tip current integration scheme for calculating the effective tip area of a field emitter. Chapter 3 explores the concept of space-charge limited current for planar, cylindrical, and spherical emitter tip geometries. Chapter 4 presents some design choices in selecting an equivalent circuit for resonant or tuned field emitter amplifiers. Chapter 5 discusses how an amplifier model for a field emitter amplifier may be obtained from device transfer characteristics.

Chapter 2

A Finite Tip Current Integration Scheme for Calculating the Effective Tip Area

2.1 Introduction

There have been many attempts to relate the currents from field emitter tips to the Fowler-Nordheim equation. Most effort has focused on assuming a work function for the emitter material and then solving the Fowler-Nordheim equation for the field enhancement factor and the emitting area. This is done by fitting the (I/V^2) vs $log(1/V)$ curve by linear regression and using the slope and intercept to calculate values for the field enhancement factor and the emitting area. Some problems with this approach are obvious. For instance, the Fowler-Nordheim equation has constants which are experimentally determined for different materials. Important dimensions such as the tip radius are not accurately known and must be assumed. Also, the work function for most materials is not accurately known. Perhaps the major drawback is the possible inadequacy of the Fowler-Nordheim equation to model this situation at all due to the assumptions that are inherent in its solution. In addition, the radius of curvature of the emitter tips is smaller than an electron deBroglie wavelength in Silicon, and there is the yet unquantified effect of the thin tip oxide layers on the work function.

Assuming that the Fowler-Nordheim equation is a good model for calculating the current from the tip, there remains the matter of the tip enhancement factor and the emitting area. The electric field is not uniform across the tip. Thus, using the maximum value of the electric field to calculate the field enhancement factor will underestimate the emitting area. In this paper, a new way of calculating the effective tip area is proposed. The scheme is based on finding the electric field at a number of points along the tip and using these values to calculate the current densities. The current densities are multiplied by the area to which they correspond and summed to provide the total tip current. This

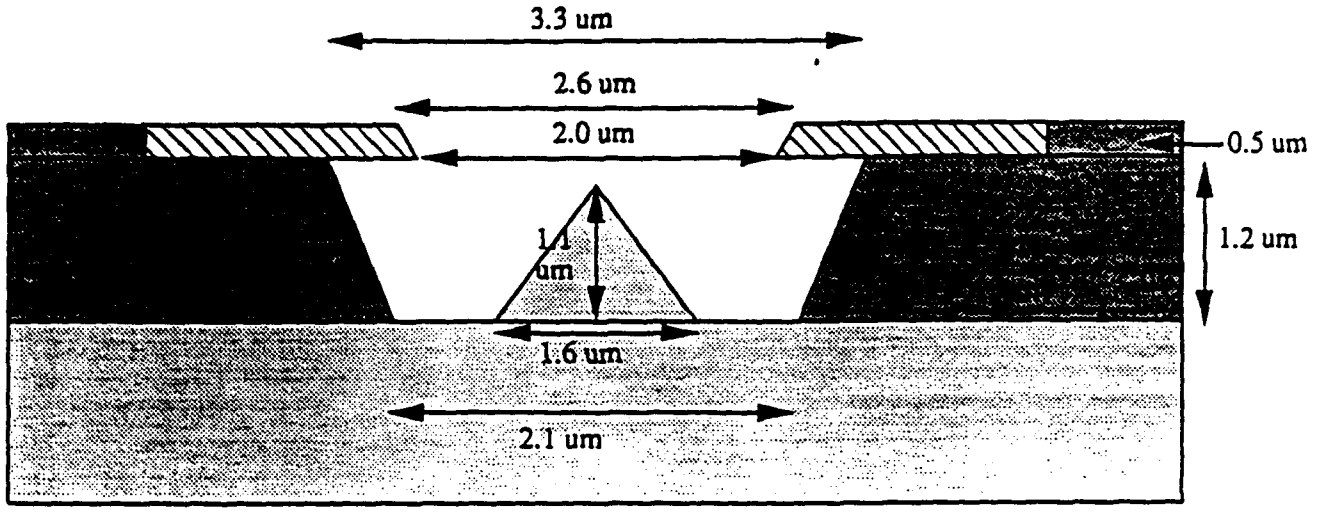

Figure 2.1: Field emitter cone geometry.

tip current can be divided by the current density calculated from the maximum field to find an effective emitting area.

2.2 Theory

We begin with the assumption that the tip radius and work function of the material are known. The geometry is shown in Figure 2.1 and is circularly symmetric, i.e. the figure is a body of revolution. The tip of the field emitter is a half-sphere of radius 100 Angstroms(Å). Other dimensions are shown. The electric field distribution around the top of the field emitter can be calculated using a finite element program. The electric field at the tip of a field emitter is not uniform, therefore, the current extracted from the tip is a function of position. In order to calculate a more meaningful value for the effective tip emitting area, it is necessary to take this into account. The scheme we choose takes advantage of the cylindrical symmetry of the emitter tip. For a given electric field, the current density extracted from an emitter tip is governed by the Fowler-Nordheim (FN) equation

$$J = 1.40 \times 10^{-6} \frac{E^2}{\phi} exp\left[-6.83 \times 10^{7} \frac{\nu \phi^{3/2}}{E}\right] \tag{2.1}$$

In the above equation, E is the electric field in V/cm, ϕ is the work function of the emitter in eV, and ν is a unitless parameter given by

$$\nu = 0.95 - 1.217 \times 10^{-7} \frac{E}{\phi} \tag{2.2}$$

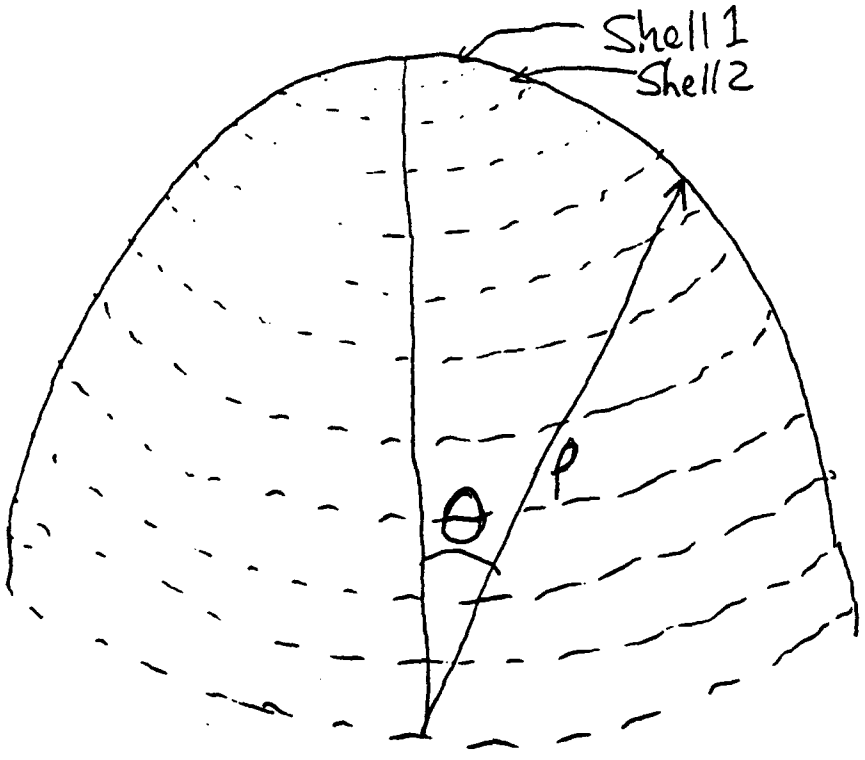

Figure 2.2: Field emitter tip divided into spherical rings.

In order to provide a more accurate picture of the current distribution, the emitter tip is broken up into sixteen spherical rings, as shown in Figure 2.2. The rings are centered every six degrees as measured by the angle θ. The top ring is actually a cap that extends from $\theta = 0°$ to $\theta = 3°$. Its area is $2\pi r^2[\cos(0°) - \cos(3°)] = 8.61 \times 10^{-15}\ cm^2$. The next ring extends from $\theta = 3°$ to $\theta = 9°$ and has an area of $2\pi r^2[\cos(3°) - \cos(9°)] = 6.87 \times 10^{-14}\ cm^2$. Each succeeding ring also covers six degrees except the last, which goes from $\theta = 87°$ to $90°$. The ring areas are calculated in an analogous manner. The electric fields at the center of each ring are determined with a finite element electromagnetics program. Next, the current density from each ring is calculated using the FN equation and multiplied by the ring area to provide the total current from each ring. These currents are summed for the total tip current.

The effective emitting area can be estimated in at least three ways. One is to simply add the areas from each ring that provides a significant portion of the total current. Another is to define the tip area as the area of the rings that include 90%(or some other percentage) of the total current. A third measure of the effective tip area is to divide the total current calculated in the above manner by the current density as calculated from the FN equation from the maximum electric field. This does not necessarily give a physically meaningful tip area, but it does provide a way of comparing these results with the usual results.

Table 2.1: Electric field magnitude, current density, ring area, and total current for each ring. Tip radius is 100 Åand gate voltage is 200 V.

Ring	θ	E_{mag}	J	Ring Area	I(ring)
#	degrees	$\times 10^9 V/m$	$\times 10^3 A/cm^2$	$\times 10^{-12} cm^2$	$\mu A/tip$
1	0	5.12	1840	.0086	.0158
2	6	5.08	1670	.0687	.1147
3	12	5.24	2440	.1367	.3335
4	18	5.14	1930	.2032	.3922
5	24	5.08	1670	.2675	.4467
6	30	4.96	1240	.3288	.4077
7	36	4.82	857	.3866	.3313
8	42	4.68	582	.4401	.2561
9	48	4.48	332	.4887	.1574
10	54	4.32	193	.5321	.1027
11	60	4.22	138	.5696	.0786
12	66	3.66	15.3	.6008	.0092
13	72	3.36	3.54	.6255	.0022
14	78	3.08	0.711	.6433	.0005
15	84	2.36	0.002	.6541	.0000
16	90	1.80	0.000	.3288	.0000

2.3 Results

The results are interesting. Defining an effective emitting area can be at once misleading and useful. The major point to come from this study is that even for different geometries 90% of the current comes from approximately the upper 45o of the tip. This corresponds to an area of about $2r^2$ where r is the radius of the tip. Additionally, 63%, or $(1 - e^{-1})$, of the current comes from an area of about r^2.

It is important to point out that regardless of how the emitting area is defined, it will change with voltage, work function, tip radius, or just about anything else. Therefore, the concept is much more nebulous than it first appears. This study has given us an opportunity to check the ideas regarding the emitting area. Further experimental work may help determine which definition for the emitting area is most useful.

Table 1 shows the results from a representative run. In this example, the tip radius is 100 Å, the gate voltage is 200 V, and the work function of the emitter material is assumed to be 4.05 eV. The total current from the tip, found by summing the last column, is 2.65 μA. It can be shown that 90% of the current comes from upper part of the cone with a half-angle of about 45°, as stated previously. Data from a tip radius of 50 Åat gate voltages of 150 V and 200 V show similar results.

Chapter 3

Space-Charge Limited Current for Planar, Cylindrical, and Spherical Geometries

3.1 Introduction

The current that flows from one conductor to another conductor at a different potential is limited by the space-charge effect. The space-charge effect is due to the shielding that occurs from the charged particles. As a certain density of charged particles is reached, the electric field that is accelerating them is blocked by this sheet of charge. This paper examines the space-charge limiting effect for planar, cylindrical, and spherical geometries. The governing equation for planar conductors, the Child-Langmuir Law, is derived from Poisson's equation in the next section.

3.2 The Child-Langmuir Law

The space-charge limiting case describes the maximum current density that can be transmitted from one conductor to another. Under certain initial conditions, the current is limited by the shielding of other charged particles between the two conductors. At a critical value, the charge density shields particles from the electric field. The derivation for planar conductors, which yields the Child-Langmuir Law, is carried out below. The geometry referred to is shown in Figure 1.

Starting with Poisson's equation in one-dimension

$$\Delta^2\phi = \frac{d^2\phi}{dx^2} = -\frac{\rho}{\epsilon} \tag{3.1}$$

we assume that there is a sheet of particles, electrons for instance, at x=0 with no initial velocity. They are subjected to an electric field set up by the zero potential surface they

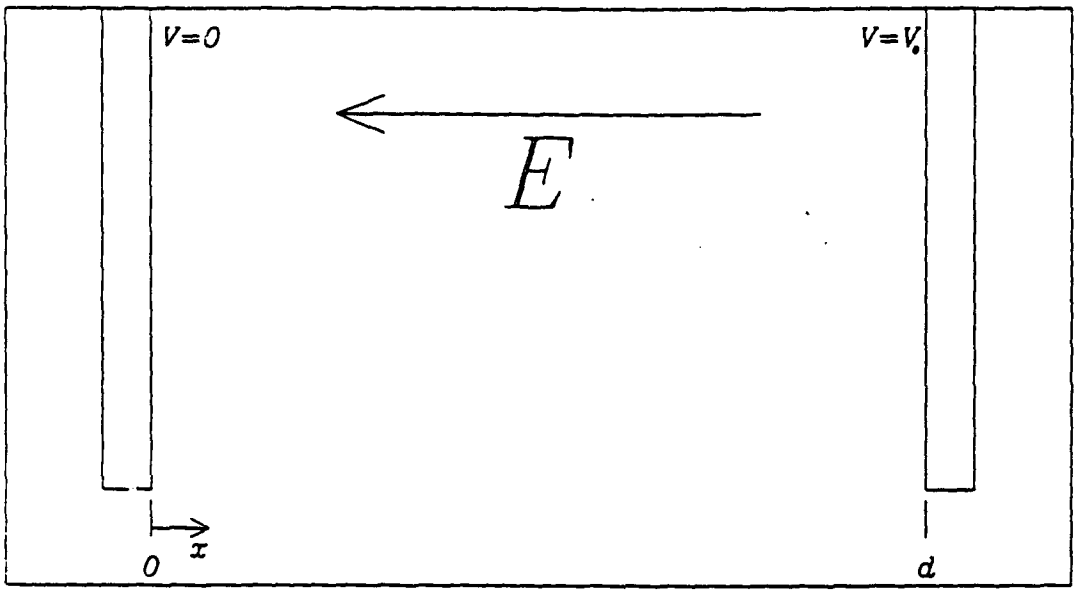

Figure 3.1: Planar conductor geometry used to derive the Child-Langmuir Law.

are on and the constant potential at a distant plane, x=d. As it begins to accelerate, the kinetic energy of such an electron can be related to its velocity and potential by

$$\frac{1}{2}mv^2 = q\phi \quad ==> \quad v = \sqrt{\frac{2q\phi}{m}} \tag{3.2}$$

For a particle density ρ and velocity v the current density is given by $J = \rho v$. Substituting these expressions into equation (1) gives,

$$\frac{d^2\phi}{dx^2} = -\frac{\rho v}{\epsilon}\sqrt{\frac{m}{2q\phi}} = \frac{J}{\epsilon}\sqrt{\frac{m}{2q\phi}} \tag{3.3}$$

Multiplying through by $d\phi$, we get

$$\frac{d\phi}{dx}\frac{d^2\phi}{dx} = \frac{J}{\epsilon}\sqrt{\frac{m}{2q}}\,\phi^{-1/2}\,d\phi \tag{3.4}$$

To integrate the expression we need to provide appropriate limits of integration. The limits of the integration in the equation below correspond to an initial condition that the electrons at the first conductor have no initial velocity. Thus, when $\phi = 0$ their velocity is also zero as is the derivative of the potential $d\phi/dx$.

$$\int_0^{\frac{d\phi}{dx}} \frac{d\phi}{dx}\frac{d^2\phi}{dx} = \int_0^{\phi} \frac{J}{\epsilon}\sqrt{\frac{m}{2q}}\,\phi^{-1/2}\,d\phi \tag{3.5}$$

Integrating yields

$$\frac{1}{2}\left(\frac{d\phi}{dx}\right)^2 = \frac{J}{\epsilon}\sqrt{\frac{m}{2q}}\frac{\phi^{1/2}}{1/2} \tag{3.6}$$

or

$$\left(\frac{d\phi}{dx}\right)^2 = \frac{4J}{\epsilon}\sqrt{\frac{m}{2q}}\phi^{1/2} \tag{3.7}$$

Taking the square root of the last equation yields

$$\left(\frac{d\phi}{dx}\right) = 2\sqrt{\frac{J}{\epsilon}}\left(\frac{m}{2q}\right)^{1/4}\phi^{1/4} = K_1\phi^{1/4} \tag{3.8}$$

where K_1 replaces the constants. This equation can be solved for the relationship between the potential applied and the current. Integrating the above equation between x=0 and x=d, where the potential changes from 0 to V_0, yields

$$\int_0^{V_0}\phi^{-1/4}d\phi = \int_0^d K_1 dx \tag{3.9}$$

$$\frac{4}{3}V_0^{3/4} = K_1 d \tag{3.10}$$

$$V_0^{3/2} = \frac{9}{16}K_1^2 d^2 = \frac{9}{4}\frac{J}{\epsilon}\left(\frac{m}{2q}\right)^{1/2} d^2 \tag{3.11}$$

Thus, the current density is given by

$$J = \frac{4\epsilon}{9}\left(\frac{2q}{m}\right)^{1/2}\frac{V_0^{3/2}}{d^2} \tag{3.12}$$

This current density is the maximum current density that can be transmitted between the plates for the voltage V_0, because it is calculated assuming that an infinite amount of current is available at x=0. In terms of current, for plates of area A, a first approximation neglecting edge effects gives

$$I = \frac{4\epsilon}{9}\left(\frac{2q}{m}\right)^{1/2}\frac{AV_0^{3/2}}{d^2} \tag{3.13}$$

This equation is called the Child-Langmuir Law.

As can be seen from the Child-Langmuir Law, the space–charge limited current varies as the 3/2-power of the voltage difference applied between the plates and is inversely proportional to the square of the plate separation distance. Similar relationships hold for cylindrical and spherical geometries, but the equations are more difficult to derive. In general, the 3/2-power rule for space–charge limiting holds for all geometries [1]. The expressions for space-charge limited current for cylindrical and spherical geometries are given in the next two sections.

3.3 Cylindrical conductors.

The development for cylindrical conductors is similar to that of the previous section. The geometry referred to is shown in Figure 2, where r_e is the radius of the emitter, r_a is the radius of the anode, and r is a variable location in between the two. (The same geometry is used in the section for spherical geometries.) The space-charge limited current density at the anode is given by

$$J_{SCL}(r_a) = \frac{4\epsilon}{9}\left(\frac{2q}{m}\right)^{1/2}\frac{V_0^{3/2}}{r_a^2\beta^2} \tag{3.14}$$

where

$$\beta = \gamma - \frac{2}{5}\gamma^2 + \frac{11}{120}\gamma^3 - \frac{47}{3300}\gamma^4 + \cdots \tag{3.15}$$

$$\gamma = \ln\left(\frac{r_a}{r_e}\right) \tag{3.16}$$

β can be approximated by

$$\beta \approx 1 + 0.9769\left(\frac{r_a}{r_e}\right)^{2/3}\sin\left[\frac{\sqrt{2}}{3}\ln\left(\frac{r_a}{11.93r_e}\right)\right] \tag{3.17}$$

for $\gamma > 4$, and

$$\beta^2 \approx 4.6712\left(\frac{r_a}{r_e}\right)\left[\log\left(\frac{r_a}{1.414r_e}\right)\right]^{3/2} \tag{3.18}$$

for small γ ($\gamma \ll 1$). Values for β^2 are tabulated on page 178 of the book by Spangenberg [2].

The SCL current is expressed in terms of the SCL current density times the area of the cylinder, namely $2\pi r_a$ times the length, L.

$$I_{SCL} = \frac{4\epsilon}{9}\left(\frac{2q}{m}\right)^{1/2}\frac{V_0^{3/2}}{r_a^2\beta^2}(2\pi r_a)L = \frac{8\pi\epsilon}{9}\left(\frac{2q}{m}\right)^{1/2}\frac{V_0^{3/2}}{r_a\beta^2}L \tag{3.19}$$

This value for the space-charge limited current assumes that the current is emitted by a full cylinder. If only part of the cylinder is emitting the current, or if the geometry includes only part of the cylinder, it is only necessary to include a fraction of the current given by the above equation. If the cylinder is not full, but instead emits only over a half-angle θ, the current is given by

$$I_{SCL} = \frac{8\pi\epsilon}{9}\left(\frac{2q}{m}\right)^{1/2}\frac{V_0^{3/2}}{r_a\beta^2}L\frac{\theta}{180^\circ} \tag{3.20}$$

$$I_{SCL} = 14.66\frac{V_0^{3/2}}{r_a\beta^2}L\frac{\theta}{180^\circ}\ (\mu A) \tag{3.21}$$

Once again, this is the natural first approximation of the problem which does not include edge effects.

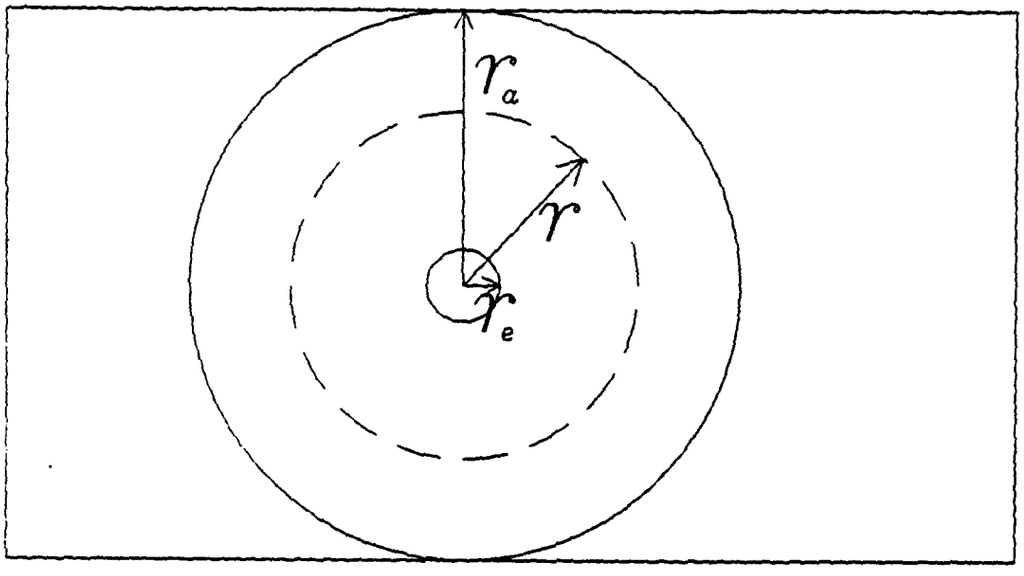

Figure 3.2: Geometry for cylindrical and spherical conductors. r_a is the anode radius, r_e is the emitter radius, and r is the variable distance.

3.4 Spherical geometries

The SCL current density for spherical electrodes is derived in a similar manner to that for cylindrical conductors. Once again, I will only show the result here. The geometry shown in Figure 2 applies, although now it is the cross section of a spherical body of revolution. The SCL current density is

$$J_{SCL}(r_a) = \frac{4\epsilon}{9}\left(\frac{2q}{m}\right)^{1/2}\frac{V_0^{3/2}}{r_a^2\alpha^2} \tag{3.22}$$

where

$$\alpha = \gamma - 0.3\gamma^2 + 0.075\gamma^3 - 0.01432\gamma^4 + 0.00216\gamma^5 - \cdots \tag{3.23}$$

$$\gamma = \ln\left(\frac{r_a}{r_e}\right) \tag{3.24}$$

For large γ, $(r_a \gg r_e)$

$$\alpha^2 \approx \frac{2}{3}\gamma + 0.5158\log(3.885\gamma) \tag{3.25}$$

For values of γ less than about 4, $(r_e \gg r_a)$

$$\alpha^2 \approx \left[1.11\left(\frac{r_a}{r_e}\right) - 1.64\right]^{3/2} \tag{3.26}$$

Values for α^2 are tabulated on page 825 of the book by Spangenberg [2] and in the article by Langmuir and Blodgett [3].

Once again, the SCL current is expressed as the current density times the area of the sphere, $4\pi r_a^2$.

$$I_{SCL} = \frac{4\epsilon}{9}\left(\frac{2q}{m}\right)^{1/2}\frac{V_0^{3/2}}{r_a^2\alpha^2}4\pi r_a^2 = \frac{16\pi\epsilon}{9}\left(\frac{2q}{m}\right)^{1/2}\frac{V_0^{3/2}}{\alpha^2} \tag{3.27}$$

$$I_{SCL} = 29.33\frac{V_0^{3/2}}{\alpha^2} \quad (\mu A) \tag{3.28}$$

If the sphere only emits from a half-angle of θ, the current is given by

$$I_{SCL} = \frac{16\pi\epsilon}{9}\left(\frac{2q}{m}\right)^{1/2}\frac{V_0^{3/2}}{\alpha^2}\left(\frac{1-\cos(\theta)}{2}\right) \tag{3.29}$$

Using typical parameters of $r_e = 100$ Å, a gate voltage of 150 V, and a gate to emitter spacing of $r_a = 1\ \mu m$, we have $r_a/r_e = 100$ and $\alpha^2 = 3.652$. Assuming the tip emits with a half-angle of 45°, the space-charge limited (SCL) current is 2.16 mA. This is about three orders of magnitude larger than the current that would be emitted by an emitter with a work function of 4.05 eV and the standard geometry. Thus, the SCL for field emitters does not appear to be a significant limiting factor at this time.

1. Langmuir, I. L. and K. T. Compton, *Electrical Discharges in Gases*, **Rev. Mod. Phys.**, Vol. 3, pp. 191-251, April 1931.

2. Spangenberg, K. R., Vacuum Tubes, McGraw-Hill Book Company, New York, 1948.

3. Langmuir, I. L. and K. Blodgett, *Currents Limited by Space Charge between Concentric Spheres*, **Phys. Rev.**, Vol. 24, p. 53, July 1924.

Chapter 4

Resonant or Tuned Field Emitter Amplifiers

4.1 Equivalent Circuit and Gain at Resonance

An equivalent circuit of the field-emitter amplifier (FEA) is shown in Fig. 4.1a, where the interelectrode capacitances and resistances (R_1 and C_1 on the input side, and R_2 and C_2 on the output side) are indicated. The inductances L_1 and L_2 are added external to the device for the purpose of resonating with, and therefore nulling out the effects of, C_1 and C_2 at any selected frequency f_0. The conditions at resonance (f_0), the gain versus frequency, the frequency bandwidth, and the physical realization of the tuned amplifier will be examined.

For analysis, Fig. 4.1 is redrawn as in Fig. 4.2, where: $Z_S = R_S + j\omega L_1$, $Z_1 = R_1/(1 + j\omega C_1)$, $Z_2 = R_2/(1 + j\omega C_2)$, and $Z_L = R_L + j\omega L_2$. The transducer power gain, in terms of the ABCD parameters of the network between Z_S and Z_L in Fig. 4.2, is,

$$G_t = \frac{4R_S R_L}{|AZ_L + B + CZ_S Z_L + DZ_S|^2} \tag{4.1}$$

where, for the equivalent circuit in Fig. 4.2,

$$A = \frac{-1}{g_m Z_2},\ B = \frac{-1}{g_m},\ C = \frac{-1}{g_m Z_1 Z_2},\ D = \frac{-1}{g_m Z_1} \tag{4.2}$$

Substitution yields,

$$G_t = \frac{4g_m^2 R_S R_L}{\left|\left(1 + \frac{Z_S}{Z_1}\right)\left(1 + \frac{Z_S}{Z_2}\right)\right|^2} \tag{4.3}$$

4.1.1 Gain at resonance

If Z_S and Z_L are adjustable, then a conjugate impedance match may be obtained at the input and output of the network in Fig. 4.2, so that $Z_S = Z_1^*$ and $Z_L = Z_2^*$. This

occurs at one particular frequency where $\omega_0 L_1 = 1/(\omega_0 C_1)$ and $\omega_0 L_2 = 1/(\omega_0 C_2)$, and $f_0 = \omega_0/(2\pi)$ is referred to as the resonant frequency. Thus, at resonance, where the source and load impedances are conjugately matched, the transducer power gain from (4.3) is,

$$G_t = 4g_m^2 R_S R_L = g_m^2 \frac{R_1 R_2}{4} \tag{4.4}$$

For this to be true, or for the conjugate match to occur, requires that,

$$\frac{L_1}{R_S} = R_1 C_1 \tag{4.5}$$

$$R_S = \frac{R_1}{1 + (\omega_0 R_1 C_1)^2} = \frac{R_1}{1 + g_m^2 R_1^2 \left(\frac{f_0}{f_T}\right)^2} \tag{4.6}$$

and

$$R_L = \frac{R_2}{1 + (\omega_0 R_2 C_2)^2} = \frac{R_2}{1 + g_m^2 R_2^2 \left(\frac{f_0}{f_T}\right)^2} \tag{4.7}$$

where $f_T = g_m/(2\pi C_1)$. As an example, assuming that a conjugate match has been achieved, let $g_m = 0.025$ S and $R_1 = R_2 = 500\Omega$. Then, from (4.4),

$$G_t = g_m^2 \frac{R_1 R_2}{4} = 39.04 \tag{4.8}$$

Note from (4.6) and (4.7) that R_S and R_L may need to be quite small at high frequencies in order for a conjugate match to occur. This requirement may severely restrict the amplifier network shown in Fig. 4.2, where the external inductance is added in series with R_S and R_L. Since it is the designer's choice, the external inductance may be added in parallel at the input and output as illustrated in Fig. 4.3. The network in Fig. 4.3 may be analyzed using the same equations, (4.1), (4.2), and (4.3), if we let $Z_S = R_S$, $Z_L = R_L$, let Z_1 be the parallel combination of R_1, L_1, C_1, as

$$Z_1 = \frac{R_1}{1 + j\left(\omega C_1 - \frac{1}{\omega L_1}\right)} \tag{4.9}$$

and let Z_2 be the parallel combination of R_2, L_2, C_2, as

$$Z_2 = \frac{R_2}{1 + jR_2\left(\omega C_2 - \frac{1}{\omega L_2}\right)} \tag{4.10}$$

Thus, at resonance, where $\omega_0 L_1 = 1/(\omega_0 C_1$ and $\omega_0 L_2 = 1/(\omega_0 C_2$, the transducer power gain of the amplifier in Fig. 4.3 is,

$$G_t = \frac{4g_m^2 R_S R_L}{\left|\left(1 + \frac{R_S}{R_1}\right)\left(1 + \frac{R_S}{R_2}\right)\right|^2} \tag{4.11}$$

Two special cases are of particular interest. If $R_1 \ll R_S$ and $R_2 \ll R_L$, the transducer gain from (4.11) becomes,

$$G_t = 4g_m^2 R_S R_L \tag{4.12}$$

If $R_1 = R_S$ and $R_2 = R_L$, the transducer gain from (4.11) becomes,

$$G_t = g_m^2 \frac{R_1 R_2}{4} \tag{4.13}$$

In the first case, if $g_m = 0.025$ S, $R_1 = R_2 = 500\Omega$, and $R_S = R_L = 50\Omega$, G_t from (4.12) is approximately,

$$G_t = 6.25 \tag{4.14}$$

In the second case, if $g_m = 0.025$ S and $R_1 = R_2 = R_S = R_L = 500\Omega$, G_t from (4.20) is,

$$G_t = 39.06 \tag{4.15}$$

Both cases yield a significant power gain. The higher gain obtained in the second case may be quite possible in practice since R_S and R_L may be made equal to R_1 and R_2, respectively, by using transformer coupling or active elements at the source and load. Note particularly that these conditions may be achieved at any frequency, as long as the proper values of L_1 and L_2 are added to resonate with C_1 and C_2. Thus, by nulling out the effects of C_1 and C_2 with L_1 and L_2 at $f = f_0$, the highest power gain that the amplifier is capable of producing $(g_m^2 R_1 R_2/4)$ may be realized at any selected frequency f_0.

A third variation of the original equivalent circuit in Fig. 4.1 will be used to illustrate an unfavorable situation that should be avoided by careful design of the amplifier circuit. This equivalent circuit is shown in Fig. 4.4, where R_1 is assumed large enough to be neglected for a simpler analysis, and the inductance L_1 is added in series at the input. The series resistance R_1' is the summation of resistance in L_1 and any series resistance contributed by wire bonds and bulk material in the gate region. The less critical output circuitry is kept with all components in parallel.

Once again, the network in Fig. 4.4 may be analyzed using (4.1), (4.2), and (4.3), if we let $Z_S = R_S + j\omega L_1$, $Z_L = R_L$,

$$Z_1 = R_1' - j\frac{1}{\omega C_1} \tag{4.16}$$

and

$$Z_2 = \frac{R_2}{1 + jR_2\left(\omega C_2 - \frac{1}{\omega L_2}\right)} \tag{4.17}$$

Thus, at resonance, where $\omega_0 L_1 = 1/(\omega_0 C_1$ and $\omega_0 L_2 = 1/(\omega_0 C_2$, the transducer power gain of the amplifier in Fig. 4.4 is,

$$G_t = \frac{4g_m^2 R_S R_L \left(1 + \frac{1}{\omega_0^2 C_1^2}\right)}{(R_S + R_1')^2 \left(1 + \frac{R_L}{R_2}\right)^2} \tag{4.18}$$

Again, two special cases may be of particular interest. If $R_S = R_L = R_1'$ and $R_L \ll R_2$, the transducer gain from (4.18) becomes,

$$G_t \doteq g_m^2 \left(1 + \frac{1}{\omega_0^2 C_1^2}\right) \cong \frac{g_m^2}{\omega_0^2 C_1^2} = \left(\frac{f_T}{f_0}\right)^2 \tag{4.19}$$

If $R_1' = R_S$ and $R_2 = R_L$, the transducer gain from (4.18) becomes,

$$G_t = g_m^2 \frac{R_2}{4R_1'} \left(1 + \frac{1}{\omega_0^2 C_1^2}\right) \cong g_m^2 \frac{R_2}{4R_1' \omega_0^2 C_1^2} = \frac{R_2}{4R_1'} \left(\frac{f_T}{f_0}\right)^2 \tag{4.20}$$

where $f_T = g_m/(2\pi C_1)$, and it is seen that in both cases the gain decreases as frequency increases. In the first case, if $g_m = 0.025$ S and $C_1 = 4$ pF, $G_t = 1$ at $f_0 = 0.995$ GHz. In the second case, $R_2 = 500\Omega$, $R_1' = 50\Omega$, and $C_1 = 4$ pF, $G_t = 1$ at $f_0 = 1.57$ GHz.

4.2 PHYSICAL REALIZATION OF TUNED AMPLIFIER

The inductances L_1 and L_2, that are used to null out the effects of C_1 and C_2 at any selected frequency, are easily incorporated into the microstrip circuit that will be used in testing the field-emitter amplifiers. Fig. 4.5 shows the microstrip circuit with a packaged amplifier (gate, emitter, and collector leads) to be inserted. The input and output RF lines are of 50Ω characteristic impedance ($w_0 = 2.44$ mm on the 0.723 mm thick, RT Duroid dielectric substrate). The open-circuited stubs of physical length l_1 and l_2 are between one-quarter and one-half wavelength long at f_0 and form the inductances L_1 and L_2. For example calculations these stubs will also be assigned a characteristic impedance of 50Ω, which can be changed to make the physical lengths longer or shorter if desirable. The physical lengths l_1 and l_2 are:

$$l_1 = \frac{\lambda}{2\pi} \tan^{-1}\left(\frac{-Z_{01}}{\omega_0 L_1}\right) = \frac{\lambda}{2\pi} \tan^{-1}\left(-Z_{01}\omega_0 C_1\right) \tag{4.21}$$

and

$$l_2 = \frac{\lambda}{2\pi} \tan^{-1}\left(\frac{-Z_{01}}{\omega_0 L_2}\right) = \frac{\lambda}{2\pi} \tan^{-1}\left(-Z_{01}\omega_0 C_2\right) \tag{4.22}$$

If $Z_{01} = 50\Omega$, $C_1 = 4\ pF$, and $C_2 = 2\ pF$, then:

$$l_1 = \frac{\lambda}{2\pi} \tan^{-1}\left(-1.257 f_{0G}\right) \tag{4.23}$$

and

$$l_2 = \frac{\lambda}{2\pi} \tan^{-1}\left(-0.6285 f_{0G}\right) \tag{4.24}$$

where f_{0G} is the selected frequency in GHz. At 10 GHz, $\lambda = 21.93$ mm for the 50-ohm microstrip lines in Fig. 4.5, thus, the physical lengths at 10 GHz are:

$$l_1 = 0.263\lambda = 5.77\ mm \tag{4.25}$$

and

$$l_2 = 0.275\lambda = 6.03\ mm \tag{4.26}$$

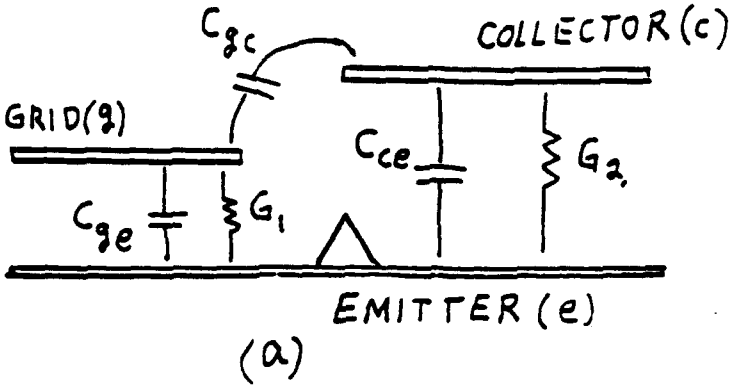

(a)

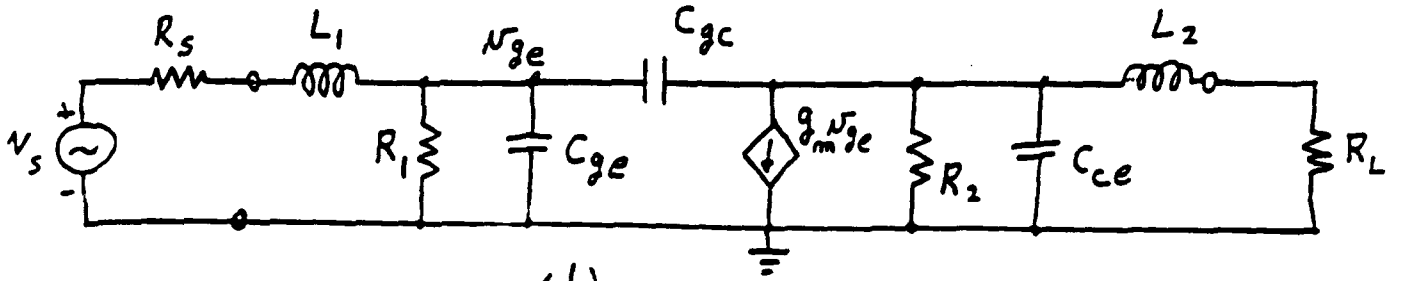

(b)

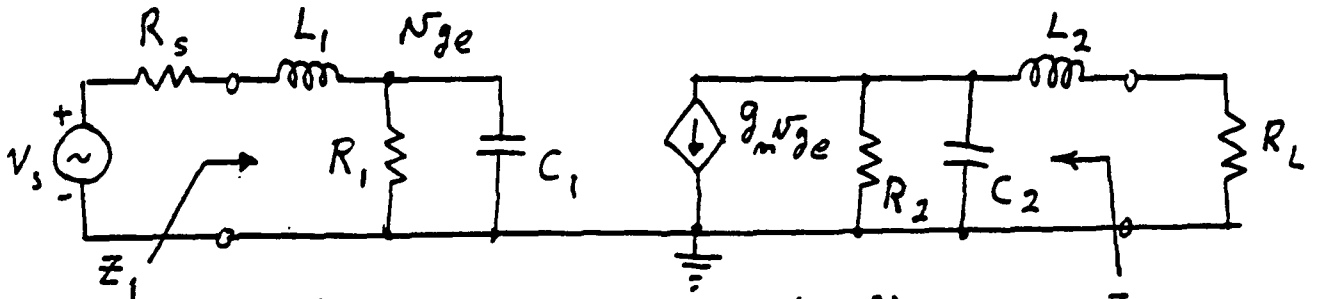

$$C_1 = C_{ge} + (1 + A) C_{gc} \qquad C_2 = C_{ce} + \left(\frac{1 + A}{A}\right) C_{gc}$$

$$A \doteq g_m \left(\frac{R_2 R_L}{R_2 + R_L}\right) \qquad R_s = R_L = Z_0$$

(c)

Figure 4.1: Device equivalent circuit evolved from interelectrode capacitances and conductances. (a) Cross-section of FEA. (b) Equivalent circuit including lead inductances, source, and load. (c) Equivalent circuit transformed by Miller's theorem.

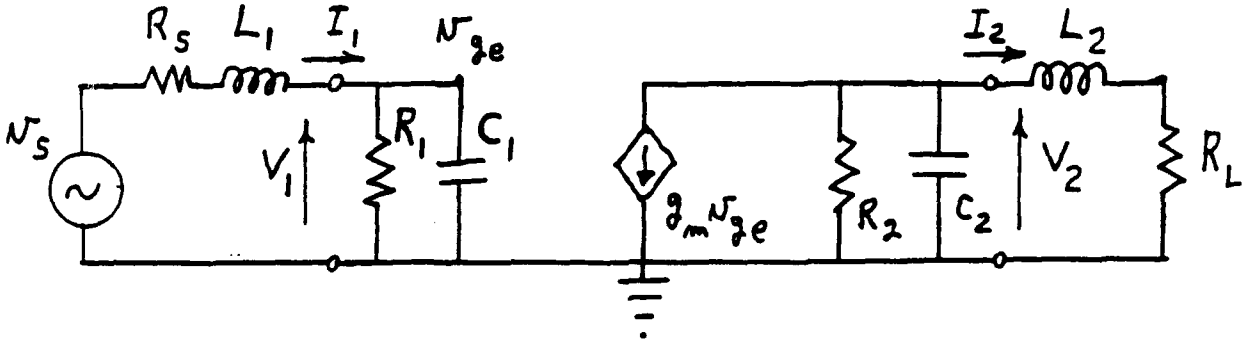

Figure 4.2: The amplifier network in Fig. 4.1 labeled for analysis.

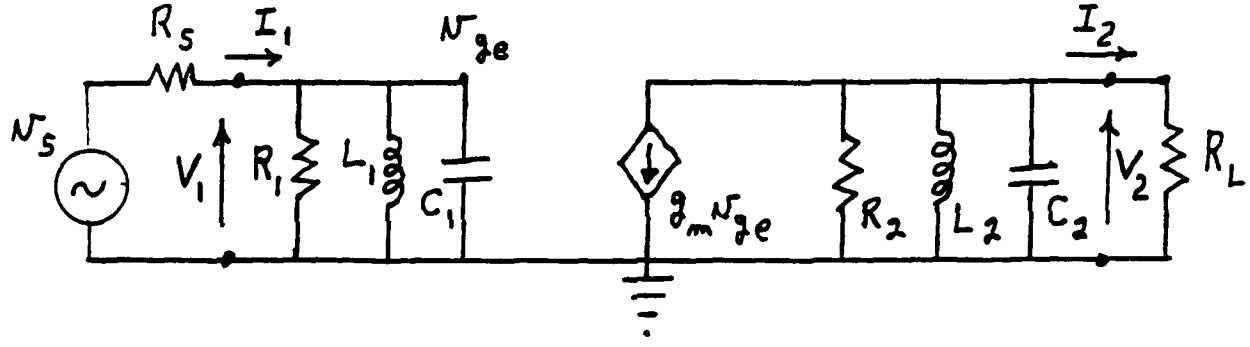

Figure 4.3: Variation of the network in Fig. 4.1 with l_1 and l_2 connected in parallel.

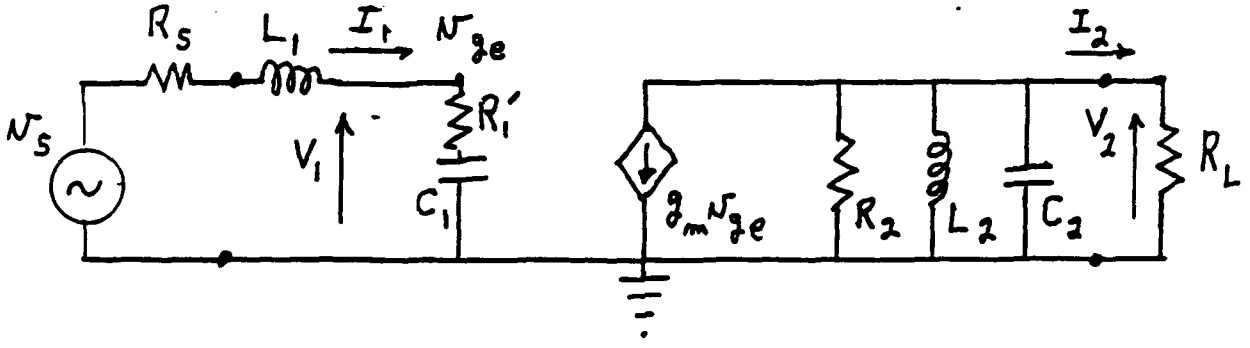

Figure 4.4: Variation of the network in Fig. 4.1 with a series resistance added at the input and R_1 large enough to be neglected.

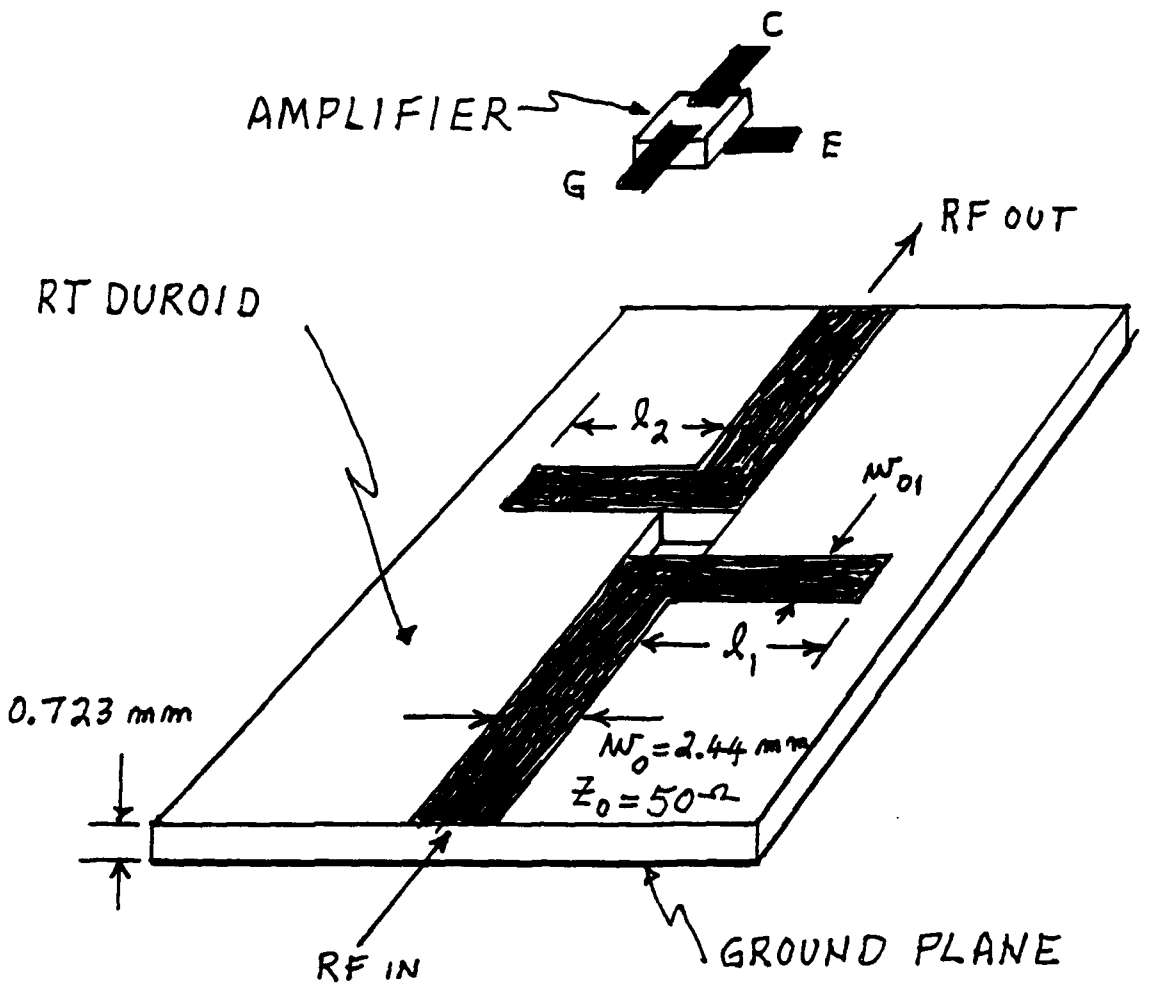

Figure 4.5: Microstrip circuit for testing the amplifier that is to be inserted into the space provided. The open-circuited stubs of length l_1 and l_2 provide the resonating inductances L_1 and L_2.

Chapter 5

Field Emitter Amplifier Modeling from Transfer Characteristics

5.1 Introduction

The output characteristics of an array of field emitters provides important information about the operating conditions under which the device provides useful gain. When the output characteristics are used to build a device model in conjunction with other experimental measurements and computational tools, information crucial to the device performance is obtained. This includes input and output impedances for matching and loading purposes, and estimates of gain and cutoff frequencies. Additionally, testing circuits and matching networks are evaluated without actually being built.

To better understand the operation of the field emitter devices, we have used output current-voltage characteristics to evaluate some of the parameters for a field emitter array circuit model. The output characteristics of a 6400-tip field emitter array are used to develop an device model which is evaluated to determine the best uses for the device. The model can be incorporated into circuit simulation programs such as PUFF and SPICE, and into mathematics programs such as Mathematica. The purpose of such a study is to understand the relative advantages of using the device in different circuit configurations and to provide information on how to build a test circuit for device testing.

5.2 Output Characteristics

In this section, we discuss the development of the device circuit model from experimentally measured output characteristics. The output characteristics of a 6400-tip array are shown in Figure 5.1 [1]. These curves are taken from experimental data presented at the Fourth International Vacuum Microelectronics Conference. They show collector current, I_C, as a function of collector to emitter voltage, V_{CE}, for different values of gate to emitter voltage, V_{GE}. These are standard curves as would be taken from a bipolar junction

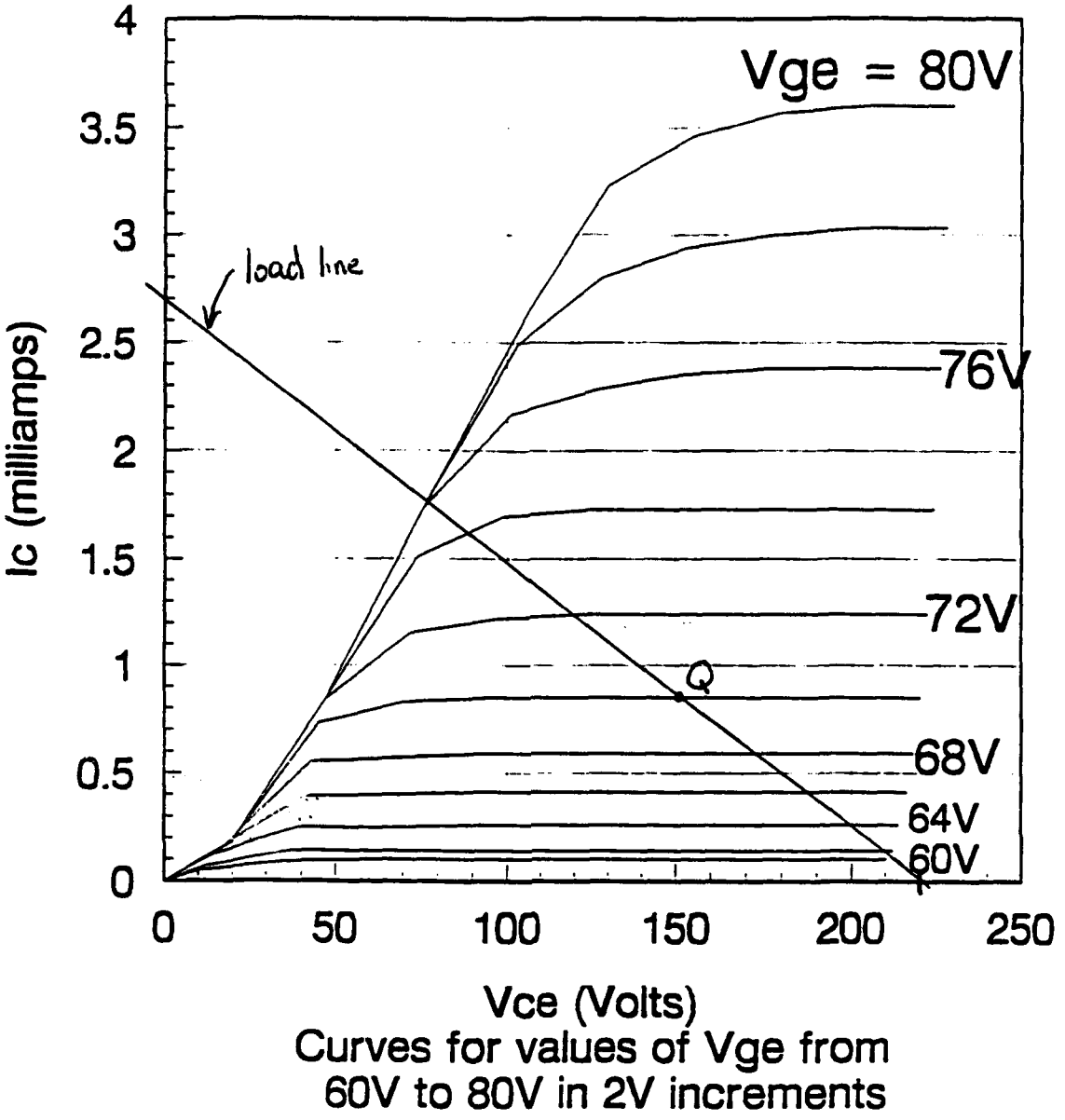

Figure 5.1: Output current-voltage characteristics.

transistor, for example. An appropriate operating point, or Q point, is determined from the curves.

For the curves of Figure 6.1, the Q point is chosen at $V_{CE} = 150\ V$ with $V_{GE} = 70\ V$ and $I_C = 0.85\ mA$. The Q point and bias circuit are taken to let the voltage and current swing relatively equally above and below it during operation as shown by the load line. The Q point and load line are marked on the figure. The bias circuit must be determined for the Q point chosen. A sample DC bias arrangement is shown in Figure 6.2 Thus, the bias is taken as $V_{CC} = 220\ V$, and $I_C = 2.67\ mA$ when $V_{CE} = 0\ V$. These choices for Q point fix the bias resistor, R_C at

$$R_C = \frac{220\ V}{2.67\ mA} = 8\Omega \quad k\Omega \tag{5.1}$$

In addition, the bias resistors R_{B1} and R_{B2} are chosen to keep V_{BE} at 70 V with $V_{CC} =$

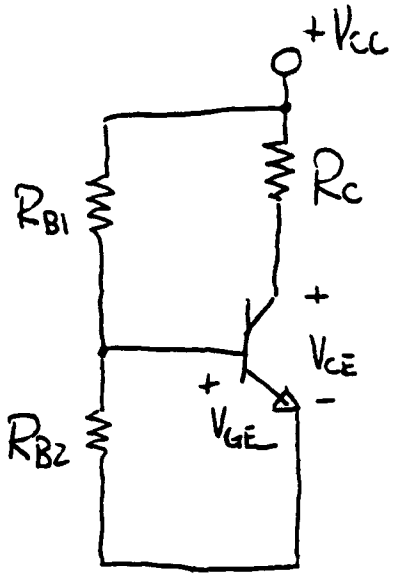

Figure 5.2: Field emitter showing the DC bias circuit.

220 V. Therefore,

$$\frac{R_{B1}}{R_{B1}+R_{B2}} = \frac{70}{220} \quad ==> \quad R_{B1} = \frac{7}{15}R_{B2} \tag{5.2}$$

The bias resistors R_{B1} and R_{B2} should be large to avoid drawing a large DC bias current. Thus, if we choose $R_{B1} = 280\ k\Omega$, then $R_{B1} = 600\ k\Omega$. Using these choices for the bias circuit, the AC circuit appears as shown in Figure 6.3. The resistor $R_B = 191\ k\Omega$ is the parallel combination of R_{B1} and R_{B2}. The gate bias resistors can be avoided if a separate DC voltage source is used on the front side in series with the AC voltage source. This is done for the ac circuit shown later.

The operation of the device in a circuit is now considered. From the load line on the graph of the output characteristics, an input voltage of $V_{GE} = 76V$ corresponds to

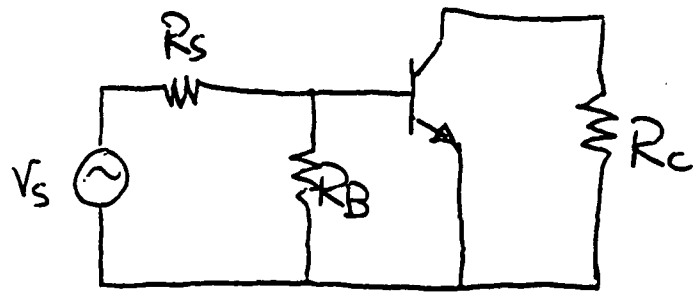

Figure 5.3: AC equivalent circuit including bias. Gate bias resistor is included.

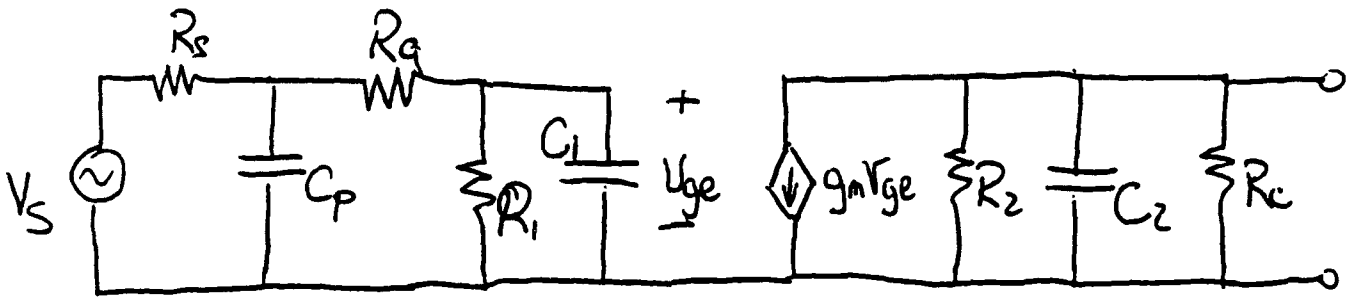

Figure 5.4: Small-signal AC equivalent circuit including important parameters. Such a model is used to predict device performance and to design testing and matching holders. In this model, the gate bias is assumed to be provided by a separate voltage source.

an output voltage of 80V. Similarly, an input voltage of 64V corresponds to an output voltage of 200V. Thus, the voltage gain of the device is

$$A_V = \frac{80 - 200}{76 - 64} = -10 \tag{5.3}$$

and the transconductance is

$$g_m = \frac{|A_V|}{R_C} = \frac{10}{82.5\ k\Omega} = 0.121\ mS \tag{5.4}$$

In addition to these parameters, the slope of the output characteristics when the current is saturated gives an indication of the conductance between the gate and the collector. Extrapolating from the $V_{GE} = 78\ V$ curve, the current is $3.02\ mA$ at $300\ V$ and $2.88\ mA$ at $0\ V$. Thus, R_2 is

$$R_2 = \frac{300\ V}{(3.02\ mA - 2.88mA)} = 2.14\ M\Omega \tag{5.5}$$

These parameters can be incorporated into a small-signal model for the field emitter array. Together with some additional information, the amplifier can be modeled in some detail. An example of the small-signal model is given in Figure 6.4. In Figure6.4 the gate bias resistor is not included because the bias is provided by a separate voltage source. This model includes many parameters, some of which may not be significant for a given useage. Some circuit parameters, such as the input and output capacitances, are determined from finite element electromagnetic analysis of the device structure. For instance, the capacitances C_1 and C_2 have values on the order of a few picofarads for the array. As determined by finite element analysis, the capacitance that corresponds to C_1 is typically about $0.4 \times 10^{-15}\ F$ per device. Therefore, a 6400-tip array should have $C_1 \approx 5\ pF$. Similarly, C_2 is approximately half of that, or $2.5\ pF$. Other parameters are

estimated similarly, either from finite element analysis, Fowler-Nordheim analysis of the field emission process, or from actual device measurements.

This model should provide important information about the performance of the device in different types of circuits. For instance, the field emitter array has possible uses as a broadband amplifier, an matched narrowband amplifier, or an oscillator, just to name a few. The modeling efforts are expected to clearly identify those areas which are particularly promising for field emitter arrays.

5.3 Future modeling efforts

As the modeling of these devices is important, much future effort will be focused on refining and revising the field emitter array model, as is evident from other chapters of this report. The model will be used to design circuitry, predict performance, and evaluate the performance of field emitter devices. It is expected that possibilities and limitations of the field emitter devices will be far better understood through the use of equivalent circuit modeling. In addition, different parameters which affect device performance can be isolated through the use of equivalent circuit models. Thus, any deviations of the experimental performance of field emitter arrays are more readily evaluated.

5.4 Reference

1. Betsui, K., "Fabrication and Characteristics of Si Field Emitter Arrays," from **Technical Digest of IVMC 91**, S. Namba, Y. Nannichi, and T. Utsumi, eds.; Published by the Program Committee of the Fourth International Vacuum Microelectronics Conference, August 22-24, 1991, Nagahama, Japan, ISBN:4-980813-45-X.

ATTACHMENT B

SIMULATION OF THIN FILM FIELD EMITTER ARRAY CATHODES

Richard True

Litton Systems, Electron Devices Division
960 Industrial Road
San Carlos, California 94070
415-591-8411

In typical field emitter arrays, individual gates have micrometer dimensions, whereas emitter tip radii are generally two orders of magnitude smaller. Because of this large size differential, it is necessary to use nonuniform meshes to accurately model such devices in a single computer run. This paper describes additions to the deformable triangular mesh finite element based beam optics code of the author, DEMEOS, which enable convenient simulation of field emitter array cathodes. The code now includes a Fowler-Nordheim emission model. As in the standard version of the code, an approximately rectangular mesh is automatically set up adjacent to the emitting surface. This feature enables the user to preselect the number of boundary points representing the emitter (which are also emission sites) for a desired level of accuracy.

Various experimental and theoretical test cases have been run. One theoretical test case is that of a hemisphere between parallel planes. Experimental cases include Spindt cathodes from the Stanford Research Institute (SRI), and silicon field emitter arrays from the Microelectronics Center of North Carolina (MCNC). The paper will include comments on the accuracy of the results as well as how the code can be used in their design. There is recent evidence that the tops of Spindt cathodes are not smooth but possess tiny crystals which protrude from the tips. The paper will discuss how geometrical boundaries can be used to readily zoom in and out so that features such as these can be explored.